11-10-2018

Two p-mode-dominated subdwarf B pulsators in binaries with F-star companions observed with K2

Michael D. Reed
Missouri State University

J. H. Telting

L. Ketzer
MSU Underraduate

J. A. Crooke
MSU Underraduate

A. S. Baran

See next page for additional authors

Recommended Citation

Reed, M. D., J. H. Telting, L. Ketzer, J. A. Crooke, A. S. Baran, J. Vos, P. Németh, R. H. Østensen, and C. S. Jeffery. "Two p-mode-dominated subdwarf B pulsators in binaries with F-star companions observed with K2." Monthly Notices of the Royal Astronomical Society 483, no. 2 (2019): 2282-2299.

Monthly Notices
of the
ROYAL ASTRONOMICAL SOCIETY

MNRAS **483,** 2282–2299 (2019)
Advance Access publication 2018 November 10

doi:10.1093/mnras/sty3025

Two p-mode-dominated subdwarf B pulsators in binaries with F-star companions observed with *K2*

M. D. Reed,[1★] J. H. Telting,[2] L. Ketzer,[1] J. A. Crooke,[1] A. S. Baran,[1,3] J. Vos,[4] P. Németh,[5,6] R. H. Østensen[1] and C. S. Jeffery[7]

[1]*Department of Physics, Astronomy and Materials Science, Missouri State University, 901 S. National, Springfield, MO 65897, USA*
[2]*Nordic Optical Telescope, Rambla José Ana Fernández Pérez 7, E-38711 Breña Baja, Spain*
[3]*Suhora Observatory and Krakow Pedagogical University, ul. Podchorąży ch 2, PL-30-084 Kraków, Poland*
[4]*Instituto de Física y Astronomía, Universidad de Valparaiso, Gran Bretana 1111, Play Ancha, Valparaiso 2360102, Chile*
[5]*Astronomical Institute of the Czech Academy of Sciences, CZ-251 65 Ondřejov, Czech Republic*
[6]*Astroserver.org, 8533 Malomsok, Hungary*
[7]*Armagh Observatory and Planetarium, College Hill, Armagh BT61 9DG, UK*

Accepted 2018 October 31. Received 2018 October 31; in original form 2018 August 3

ABSTRACT

This paper presents spectroscopic and seismic analyses of two rare hybrid pulsating subdwarf B (sdB) stars, PG 0048+091 and PG 1315−123, which are dominated by pressure (p)-mode pulsations. These are only the second and third sdB pulsators with detected frequency multiplets in both the p- and g (gravity)-mode regions. This allows an examination of the radial rotation profiles and p- and g-mode overtone spacings. Frequency multiplets indicate that PG 1315−123 rotates uniformly, as a solid body, while PG 0048+091 is rotating faster in the outer envelope. g- and p-mode overtone spacings for PG 1315−123 agree with previous findings and model predictions at 237 and ∼1000 s while those for PG 0048+091 are significantly shorter at 207 and <250 s, respectively. The cause of PG 0048+091's discrepancies is likely related to core structural differences which could be related to progenitor mass. Spectroscopic findings show that both stars lie on the hot end of the instability region and are most likely in long-period binaries with main-sequence companions. Their high temperatures challenge driving theory, which produces g-mode pulsations only at cooler temperatures. Another challenge is the appearance of pulsations with both driven and stochastic properties. Such a variety of pulsation properties makes these stars very interesting and important for understanding hot horizontal-branch stars.

Key words: stars: oscillations – subdwarfs.

1 INTRODUCTION

Pulsating subdwarf B (hereafter sdBV) stars can exhibit short pulsation periods around 1–15 minutes, which are identified with pressure (p) modes, and long periods around 45 minutes to several hours, which are ascribed to gravity (g) modes. Typical amplitudes are a few parts per thousand (ppt) or less. As sdB stars are the envelope-stripped equivalent of most horizontal-branch stars (Heber 2016), asteroseismology offers a probe of this important stage of stellar evolution. Using observed seismic features, models can constrain bulk properties (e.g. Guggenberger et al. 2016 for solar-like pulsators) and discern internal structure, composition boundaries, and processes (e.g. Degroote et al. 2010 and Metcalfe, Montgomery & Kanaan 2004 for massive and white dwarf stars, respectively). An important property of observational constraints is mode identifications from precision photometry. In that regard, the *Kepler* mission and its follow-up *K2* have been transformative for sdB seismology.

Discoveries from *Kepler* data of sdBV stars include asymptotic overtone g-mode period spacings (Reed et al. 2011) and frequency multiplets (Baran et al. 2012) which associate modes with periodicities (commonly called 'mode identifications'). Asymptotic period spacings also probe compositional discontinuities (Constantino et al. 2015) and frequency multiplets allow the determination of rotation periods (e.g. Baran et al. 2012). Mode trapping was discovered in sdBV stars by Østensen et al. (2014b) and this probes features in the resonant cavities (Constantino et al. 2015; Ghasemi et al. 2017). Stochastic features (Østensen et al. 2014a) have also been observed (though stochastic properties were previously reported by Reed et al. 2007, using ground-based data) and these probe mode stability. However, of the four published predominantly p-mode pulsators observed by the *Kepler* telescope, only

★ E-mail: mikereed@missouristate.edu

one, KIC 10139564, was a hybrid (Baran et al. 2012). The analysis of KIC 10139564 revealed frequency multiplets with consistent splittings for both the p- and g-mode pulsations which indicated uniform radial rotation rotation (as though it were a solid body). Overtone spacings in KIC 10139564 were unusual in that the g-mode spacings were either shorter, at 207 s, or longer, at 310 s, than observed in other sdBV stars (Reed et al. 2011), which average around 250 s. KIC 10139564's p-mode overtones ranged from 127 to 241 s while models indicated overtones near 1000 s. This made KIC 10139564 a very interesting yet heretofore unique object.

The best sampling delivered by the *Kepler* spacecraft (short cadence), of 58.8 s, imposes a challenge for p-mode pulsations in that periodicities may have frequencies higher than the Nyquist, which is near 8497 μHz. During the original *Kepler* mission, this was not a problem as the longer duration of observations allowed super-Nyquist frequencies to be distinguished from the sub-Nyquist reflections (Baran et al. 2012). However, K2 can only stay on target for about one quarter of a solar orbit, and so it is more difficult to distinguish super- from sub-Nyquist frequencies, though tools were investigated by Reed et al. (2018a).

In this paper we apply asteroseismic tools to two very exciting and rare hybrid pulsators. We proposed PG 1315−123 for Campaign 6 (C6) based on an NTT spectrum, which classified it as an sdB + MS binary. PG 1315−123 is EPIC 212508753 in the Ecliptic Plane Input Catalogue (Huber et al. 2016) with a *Kepler* magnitude of 15.1. We proposed PG 0048+091 (EPIC 220614972 with a *Kepler* magnitude of 14.3) for C8 as it was already a known, and very interesting, sdBV star with p-mode pulsations. Pulsations in PG 0048+091 were discovered by Koen et al. (2004), who also obtained a spectrum and determined the companion to be G0V-G2V. Multisite observations by Reed et al. (2007) detected 28 frequencies from 5200 to 11200 μHz, which pointed to an interesting and possibly unique pulsator. Frequency separations of 41.1 and 972 μHz were noted and pulsation amplitudes appeared to change on very short time-scales, leading Reed et al. (2007) to conclude that the pulsations were of a stochastic nature with damping time-scales of 4–6 hours and re-excitation time-scales of 13–21 hours. They note that the rich pulsation spectrum made such determinations difficult and the best way to solve it would be to have a long, uninterrupted time-series of data. That wish has now been answered by *K2* observations.

2 SPECTRAL ANALYSES

2.1 Low-resolution spectroscopy

As part of our follow-up spectroscopic survey (Telting et al. 2012) of *Kepler*-observed sdBV stars, we used ALFOSC at the 2.6 m Nordic Optical Telescope (see Djupvik & Andersen 2010 for a description of instrumentation), with grism #18 and a 0.5 arcsec slit providing R = 2000 resolution or 2.2Å, to obtain 5 spectra of PG 0048+091 and 12 of PG 1315−123. The instrument was equipped with CCD8 for the first 4 spectra of PG 1315−123 and later with CCD14 for the remaining spectra of both stars. The exposure time was 600 s, giving 53 < signal to noise (S/N) < 70 for PG 0048+091 and 26 < S/N < 71 for PG 1315−123.

The data were homogeneously reduced and analysed. Standard reduction steps within IRAF included bias subtraction, removal of pixel-to-pixel sensitivity variations, optimal spectral extraction, and wavelength calibration based on arc-lamp spectra. The target spectra and the mid-exposure times were shifted to the barycentric frame of the Solar system. A final pixel shift was applied to the velocity scale, to account for non-perfect centring of the target in the slit, based on slit images taken directly before and after the spectral exposures.

The mean spectra from each of the targets are presented in Fig. 1, and have S/N ∼ 120 (PG 0048+091) and S/N ∼ 140 (PG 1315−123). In both cases the mean spectra clearly show evidence of two binary components, typical sdB + F/G spectra. Features of the main-sequence companion include the *g* band in the wing of H γ, Ca I at 4226, and strong Ca II at 3933 Å. In the case of PG 1315−123 a clear He II line at 4686 Å indicates that the sdB star has 35 000 < $T_{\rm eff}$ < 40 000 K.

We used FXCOR in IRAF to look for velocity shifts of the sdB stars caused by the binarity. We cross-correlated the individual spectra with the average spectrum, in the regions around the best Balmer lines: H β, H γ, H δ, H 8, and H 9. For PG 0048+091 the 5 spectra were taken over a period of 13 months; the median radial velocity (RV) error is 6.4 km s^{-1}, while the RV scatter is 19 km s^{-1}. This is consistent with binary RV variations for an sdB + F/G system with a period of the order of one to a few years. For PG 1315−123 the 12 spectra were taken over a period of 16 months; the median RV error is 14 km s^{-1}, while the RV scatter is 11 km s^{-1}, pointing to an orbital period of more than 2 yr, or a low orbital inclination.

In order to decompose the average ALFOSC spectra of PG 0048+09 and PG 1315−123, each into the contributions of the sdB star and its main-sequence component, we used the spectral analysis program XTGRID (Németh, Kawka & Vennes 2012). This procedure uses local thermodynamic equilibrium (LTE) models to fit the cool companion and non-LTE models to reproduce the sdB spectrum. LTE models are interpolated from synthetic spectra drawn from the BOSZ spectral library (Bohlin et al. 2017) and non-LTE models are calculated with TLUSTY/SYNSPEC (Hubeny & Lanz 2017). The component models are combined in XTGRID to render synthetic composite spectra and fit the observations iteratively. The fit employs a standard minimization procedure following the steepest chi-square gradient in the parameter space. The spectra were fitted in their entirety (global fit) using 50 Å sampling sections. The continuum slope was adjusted to the observation in each section to ensure that the fit was based on spectral lines. We added increased weights for the He I–II lines of the sdB component and the Ca II H&K and the Mg I lines, which originate from the cool companion. XTGRID does not evaluate the validity of the decomposition, i.e. forcing the same distance to the stars. Instead, it attempts to reproduce the observed spectrum the best.

The non-LTE models for the subdwarf included H, He, C, N, and O opacities; however, only nitrogen showed a slight but measurable effect on the optical spectrum. The resolution of the ALFOSC observations did not allow us to constrain individual metal abundances from composite spectra. We tried and found that the best observational data for decomposition are a combination of low-resolution flux-calibrated spectra and high-resolution spectra. The low-resolution data constrain the component surface temperature, gravity, and flux contributions, while the high-resolution data provide the individual abundances. A single high-resolution spectrum is not always suitable to derive the subdwarf parameters. When no helium or metal lines can be identified, or a fast projected rotation smears them, the Balmer lines alone are insufficient to constrain the subdwarf with precision and it reduces the accuracy of the decomposition. There is no high-resolution spectrum available for PG 1315−123. The available UVES spectrum for PG 0048+091 (see next subsection) shows a metal-poor subdwarf. In spite of the higher resolution and larger coverage of the UVES spectrum, we

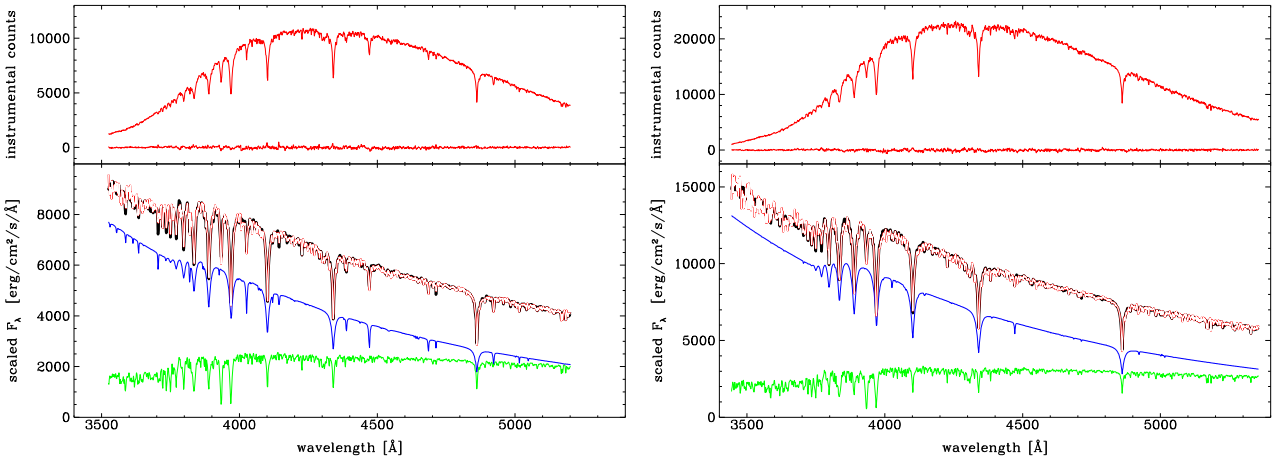

Figure 1. Spectral decomposition of PG 1315−123 (left) and PG 0048+091 (right), both based on low-resolution ALFOSC data. Top: the observed average spectrum, unnormalized, with the residuals from the decomposition fit (black in bottom panel). Bottom: the average spectrum (red), decomposed into that of an sdB (blue) and F star (green). The combined binary fit is displayed in black under the fluxed observed spectrum.

Table 1. Results of spectral decomposition as displayed in Fig. 1.

	PG 1315−123	PG 0048+091
	sdB	
$T_{\rm eff}$	36230^{+500}_{-710}	32460^{+290}_{-230}
log g	$5.61^{+0.09}_{-0.09}$	$5.77^{+0.05}_{-0.07}$
log(nHe/nH)	$-0.98^{+0.03}_{-0.15}$	$-2.30^{+0.11}_{-0.09}$
	Main-sequence companion	
$T_{\rm eff}$	6460 (+460/−560)	6270 (+840/−440)
log g	4.42 (+0.10/−0.20)	4.59 (+0.20/−0.20)
[Fe/H]	$-0.54^{+0.20}_{-0.20}$	$-0.49^{+0.20}_{-0.20}$
Dilution at 5200 Å[a]	0.48 ± 0.02	0.45 ± 0.02
Spectral type	F7V	F9V

[a]Dilution is calculated as [FMS/(FsdB + FMS)].

could not constrain the subdwarf abundances better than from the ALFOSC data alone.

The available spectroscopy does not allow us to estimate the distances to the systems. The *Gaia* Data Release 2 (DR2; Lindegren et al. 2018) provides a parallax of $\overline{\omega} = 0.945 \pm 0.043$ mas for PG 0048+091, for which Bailer-Jones et al. (2018) determine a distance of $1.025^{0.047}_{0.044}$ kpc. This distance may suffer large systematic errors due to the unresolved binarity of PG 0048+091 in *Gaia* DR2. For an orbital period around 2 yr, the components of an sdB + F binary are expected to have similar-magnitude sky motion due to binarity, as due to Earth-orbit parallax motions.

The best fits to the ALFOSC data are shown in Fig. 1, and the results are tabulated in Table 1. We found that the spectral types of the companions in both systems are late-type main-sequence F, just too cool to be in the δ Scuti p-mode instability strip, effectively excluding the source of the observed pulsations (see next sections) to be in the main-sequence stars. For both targets, we found that the main-sequence components have nearly equal flux contributions to the composite spectrum as the subdwarfs at 5400 Å.

2.2 High-resolution spectroscopy

PG 0048+091 is part of a long-term observing programme for wide sdB binaries with the UVES spectrograph mounted at the UT2 VLT telescope (Vos et al. 2018). At the time of writing, five high-resolution spectra (R ∼ 40 000) have been obtained using UVES in standard dichroic-2 437 + 760 mode. This mode covers a wavelength range of 373–499 nm in the BLUE arm and 565–946 nm in the RED arm. Exposure times were between 1000 and 1200 s, yielding S/N values between 35 and 50.

The reduction of the raw frames was conducted using the UVES Common Pipeline Library (CPL) recipes (version 5.8.2) within ESOREFLEX (version 2.8.5), the ESO Recipe Execution Tool. The standard recipes were used to optimally extract each spectrum (Larsen, Modigliani & Bramich 2012). Spectral normalization was done outside the dedicated UVES pipeline.

The current set of UVES observations is not sufficient to determine orbital parameters, but it does show long-period radial-velocity variation with lines of both components moving in opposite RV directions, confirming that PG 0048+091 is in fact a wide sdB binary with an MS companion, and not just a chance alignment of two unrelated stars. The RV variations are consistent with an orbital period of longer than two years.

To determine the spectroscopic parameters of the MS companion of PG 0048+091 the Grid Search in Stellar Parameters (GSSP) code was used. GSSP (Tkachenko 2015) is based on a grid search in the fundamental atmospheric parameters and (optionally) individual chemical abundances of the star (or binary stellar components) in question. It uses the method of atmosphere models and spectrum synthesis, which assumes a comparison of the observations with each theoretical spectrum from the grid. For the calculation of synthetic spectra, it uses the SynthV LTE-based radiative transfer code (Tsymbal 1996) and a grid of atmosphere models pre-computed with the LLMODELS code (Shulyak et al. 2004).

GSSP is used to fit the wavelength ranges of 5910–6270 and 6330–6510 Å in the RED arm of UVES. Because the sdB star is most strongly contributing in the ultraviolet (UV) and in the blue, these two ranges give the best compromise between a high S/N and a high contribution of the cool companion. There are no spectral lines of the sdB component visible in these wavelength ranges. The contribution of the sdB component is treated as a dilution factor $d = F_{\rm MS} / (F_{\rm MS} + F_{\rm sdB})$, which is included as a free parameter in the fit. A detailed description of this method, and its validation for sdB + MS binaries, is given in Vos et al. (2018).

The parameter ranges of the model grid used in GSSP are $T_{\rm eff}$ = 4000–8000 K, log g = 3.0–4.5, [Fe/H] = −0.8–0.3. The microturbulent velocity is kept fixed at 2.0 as the S/N of the spectrum is not

Table 2. The spectroscopic parameters of the MS component of PG 0048+091 as determined from UVES spectra with the GSSP algorithm. The errors are 1σ errors.

Parameter	Value
$T_{\rm eff}$ (K)	6355^{+294}_{-294}
$\log g$ (dex)	$4.50^{+0.30}_{-0.42}$
[Fe/H] (dex)	$-0.46^{+0.15}_{-0.16}$
$v_{\rm r}\sin i$ (km s^{-1})	$26^{+2.0}_{-1.6}$
Dilution at ~6200 Å	$0.59^{+0.13}_{-0.11}$

high enough to accurately determine this parameter. The projected rotational velocity is unconstrained and uses steps of 1 km s^{-1}, while the dilution factor varies between 0 and 1 in steps of 0.01. The resulting parameters with their 1σ errors are given in Table 2, and the best-fitting model is shown in Fig. 2.

Comparing the results of the main-sequence star in PG 0048+091 listed in Tables 1 and 2, we find consistent results for the stellar parameters. Taken at face value, the values of R and $v_{\rm r}\sin i$ would result in a rotation period of 2.6 ± 1.1 d for the main-sequence star for $i = 90^{\rm o}$. For lower inclinations, the rotation period would be shorter (1.8 days for $i = 45^{\rm o}$). This period is in contrast to the rotational splitting found in the pulsation multiplets of PG 0048+091(see Section 4.4), favouring the slower rotating sdB star as the source of the pulsations.

2.3 Spectral energy distribution analysis

The spectral energy distribution (SED) can be used to derive an independent set of spectral parameters for both components in an sdB + MS system. Here the photometric SED is fitted with model atmospheres to determine the effective temperature and radius of both components. The photometric measurements were obtained from the all-sky photometric surveys *Gaia* (Gaia Collaboration 2016, 2018; Evans et al. 2018; Riello et al. 2018), 2MASS (Skrutskie et al. 2006), and *WISE* (Cutri et al. 2012), as well as from the Palomar-Green catalogue of UV-excess stellar objects (Green, Schmidt & Liebert 1986). For PG 0048+091 there is also Johnson *UBV* photometry available from Koen et al. (2004).

The SED is fitted with TMAP (Tübingen NLTE Model-Atmosphere Package; Werner et al. 2003) atmosphere models for the sdB component and Kurucz atmosphere models (Kurucz 1979) for the K star. The EMCEE Monte Carlo Markov Chain sampler (Foreman-Mackey et al. 2013) was used to find the best-fitting model and the errors on the parameters. A detailed description of the SED-fitting process is given in Vos et al. (2013) and Vos et al. (in preparation).

As the surface gravity has very little influence on the SEDs, it is fixed at the spectroscopic values. The temperature of the sdB component depends greatly on the *U*-band photometry, which has a large uncertainty for both stars. This is reflected in the errors. The temperature of the cool component is better constrained. The distance is a scaling factor of the flux, and when fixed allows for an accurate determination of the radius. In the case of PG 1315−123 there is no distance estimate available, and in the case of PG 0048+091 the *Gaia* parallax is unreliable due to the binary motion. The distance resulting from an inversion of the parallax would be an underestimation of the real distance and thus the distance was not included in the fit. The derived distances and radii should therefore be seen as very rough estimates.

The resulting parameters with their 1σ errors are given in Table 3, and the best-fitting models are shown in Figs 3 and 4. For both PG 0048+091 and PG 1315−123 the temperatures of the sdB component correspond well with those derived from spectroscopy. For PG 0048+091 the temperature of the cool companion is slightly lower than that derived from spectroscopy, but both values are within errors. In the case of PG 1315−123, however, there is a large difference between the temperature derived from the SED fit and that derived from spectroscopy, with the SED temperature being some 800 K lower than that derived from spectroscopy. An SED fit for PG 1315−123 while keeping the $T_{\rm eff}$ and $\log g$ fixed to the spectroscopic values is shown on the right side of Fig. 4. The χ^2 of this fit is more than 3 times higher than that of the free fit, and the residuals show a clear pattern instead of being randomly distributed.

The reason for the difference in effective temperature of the cool component of PG 1315−123 between the spectroscopic analysis and the SED analysis is unclear. Nearby sources could have contaminated the photometry, as well as large scale infrared (IR) sources. However, there are no nearby sources and a detailed analysis of the 2MASS and *WISE* images do not reveal any large-scale structures nearby. There could be a chance alignment with a cool star that is not visible in the spectra but which causes an IR excess and leads to a colder temperature for the companion in the SED fit, but this is not very likely.

3 *K2* OBSERVATIONS AND PHOTOMETRIC VARIATIONS

Light curves were extracted from short-cadence *K2* data using our custom process described in Baran et al. (2017) and Ketzer et al. (2017), where we use aperture photometry that tracks the star's pixel position variations caused by spacecraft motion and then decorrelates the pixel–flux dependence. The data were then normalized, sigma-clipped at 5σ, and finally we multiplied the modulation intensities by a thousand so amplitudes would appear in Fourier transforms (FTs) as parts-per-thousand (ppt). The FTs are shown in the left-hand panel of Fig. 5 and to show the pulsations more clearly, a schematic representation of the pulsation spectrum is shown in the right-hand panel, without artefacts.

Both campaigns spanned 79 d with C6 between 2015 July 14 and September 30 and C8 between 2016 January 3 and March 23. Those durations provide a 1.5/T resolution of 0.22 μHz, which requires a detection threshold of 4.35σ to make it unlikely that selected peaks are caused by random noise (Bevington & Robinson 2003). For the p-mode region, the detection threshold is 0.008 ppt for PG 0048+091 and for the fainter PG 1315−123 that threshold is 0.062 ppt. At frequencies below 300 μHz, the threshold is higher because the noise also increases towards lower frequencies. In that range, the noise is calculated piece-wise using regions between pulsations and linearly interpolated in between (e.g. Reed et al. 2010, and most noticeable in Fig. 12).

To examine time evolution of the pulsations, sliding FTs (SFTs) were produced. Those for PG 0048+091 used data spanning 20 d and stepped by 2 d and those for PG 1315−123 spanned 10 d and were stepped by 2 d. An example for PG 1315−123 is shown in the top panel of Fig. 6 and indicates that amplitudes were variable. The bottom panel shows the FT of the entire data set for the same region. The peaks are split due to amplitude variations. As such, we Lorentzian fitted the frequencies and use the Lorentzian widths as the frequency uncertainty. The amplitudes we list are those of the Lorentzian fits to the entire data set.

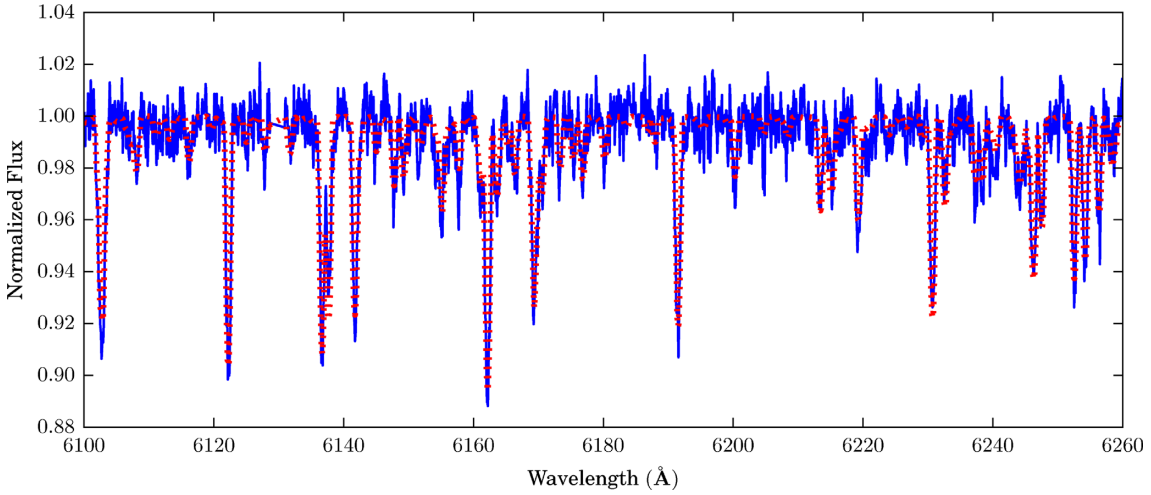

Figure 2. The observed normalized UVES spectrum of PG 0048+091 (blue full line) and best-fitting GSSP model (red dotted line) for a section of the wavelength range used to determine the spectroscopic parameters with GSSP.

Table 3. The spectroscopic parameters of PG 0048+091 and PG 1315−123 as determined by fitting model atmospheres to the photometric SED. The errors are 1σ errors.

Parameter	MS	sdB
	PG 0048+091	
$T_{\rm eff}$ (K)	6010^{+107}_{-107}	$32\,900^{+4300}_{-2600}$
R ($R_\odot$)	$1.32^{+0.45}_{-0.42}$	$0.26^{+0.11}_{-0.13}$
L ($L_\odot$)	$1.68^{+1.13}_{-0.98}$	64^{+60}_{-50}
$E(B-V)$	$0.16^{+0.07}_{-0.09}$	
d (pc)	1500^{+600}_{-500}	
	PG 1315−123	
$T_{\rm eff}$ (K)	5620^{+180}_{-150}	$36\,000^{+5000}_{-3300}$
R ($R_\odot$)	$0.91^{+0.25}_{-0.37}$	$0.13^{+0.06}_{-0.07}$
L ($L_\odot$)	$1.10^{+0.50}_{-0.60}$	$18.5^{+7.5}_{-9.5}$
$E(B-V)$	$0.18^{+0.08}_{-0.08}$	
d (pc)	1400^{+600}_{-400}	

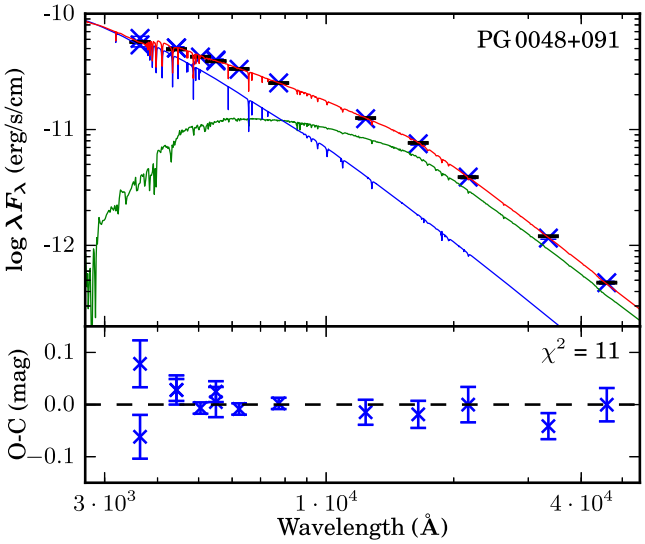

Figure 3. Photometric SED of PG 0048+091 with the best-fitting model. The observed photometry is plotted in blue crosses, while the synthetic best-fitting photometry is plotted in a black horizontal line. The best-fitting binary model is shown with a red line, while the models for the MS and sdB components are shown respectively with a green and a blue line. The residuals of the fit are plotted in the bottom panel in magnitude scale.

The left-hand panels of Fig. 6 show the FT taken up to well beyond the Nyquist frequency. It is clear from this figure that some peaks have higher amplitude in the sub-Nyquist domain and some in the super-Nyquist region. Using the highest amplitude to assign a domain to a frequency, as in Reed et al. (2018a), we obtain the reduced schematic shown in the right-hand panels of Fig. 4. Fig. 7 shows two examples for PG 0048+091. For the left-hand set, we consider the super-Nyquist frequency as the reflection, whereas in the right-hand set, we consider the super-Nyquist frequency to be intrinsic to the star.

Using those methods, we detect 208 periodicities we consider intrinsic to PG 0048+091 consisting of 18 g modes between 210 and 826 μHz (1210 and 4752 s) and 190 p modes between 1459 and 11523 μHz (86 and 685 s). We detect 62 periodicities that we consider to be intrinsic to PG 1315−123 including 16 g modes between 217 and 659 μHz (1518 to 4602 s) and 46 p modes between 5106 and 9707 μHz (103 and 196 s). These are provided in Tables 4–8 and we note that those tables do not list any of the known artefacts or Nyquist reflections. The pulsations for PG 0048+091 are nearly continuous between the g- and p-mode regions with a gap between 827 and 1459 μHz while in PG 1315−123 the gap is much larger, between 659 and 5107 μHz. We cannot distinguish whether this gap is intrinsic or caused by PG 1315−123's higher detection threshold. Also evident in Fig. 5 is that the main power in PG 1315−123 occurs at higher frequencies than for PG 0048+091.

Note that while the main-sequence companions contribute roughly half of the flux, we have not accounted for this in the listed pulsation amplitudes. In this manner, the S/N accurately reflects the pulsation detection significance and since, as described above, all of the amplitudes are variable, flux corrections would have little meaning.

Both stars have complex pulsation structures, making analyses difficult but indicating that interesting phenomena are occurring. We will begin with PG 0048+091, as it was a known pulsator prior to *K2* observations.

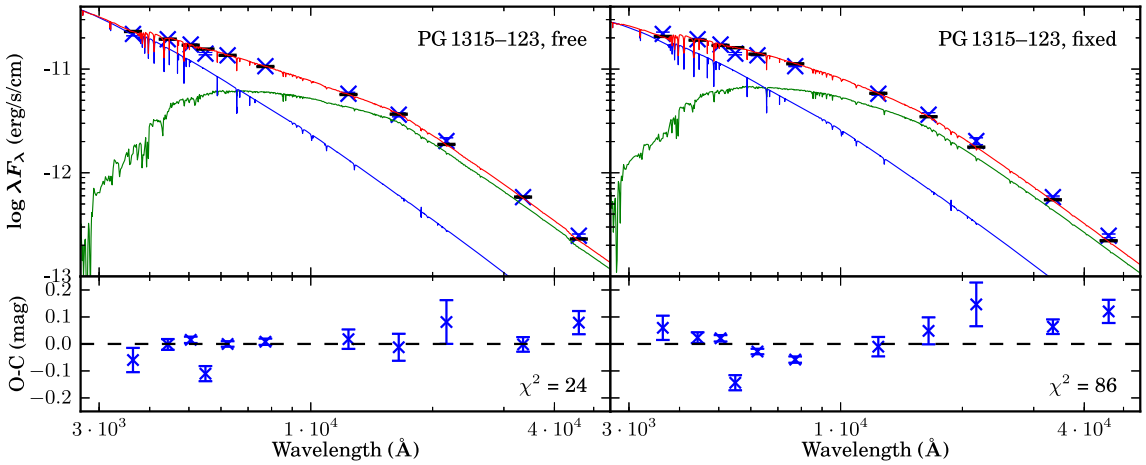

Figure 4. Photometric SED of PG 1315−123 with the best-fitting model in the case that all parameters are varied freely (left) and when the $T_{\rm eff}$ and $\log g$ are fixed to the spectroscopic values (right). The observed photometry is plotted in blue crosses, while the synthetic best-fitting photometry is plotted in a black horizontal line. The best-fitting binary model is shown with a red line, while the models for the MS and sdB components are shown respectively with a green and a blue line. The residuals of the fit are plotted in the bottom panel in magnitude scale.

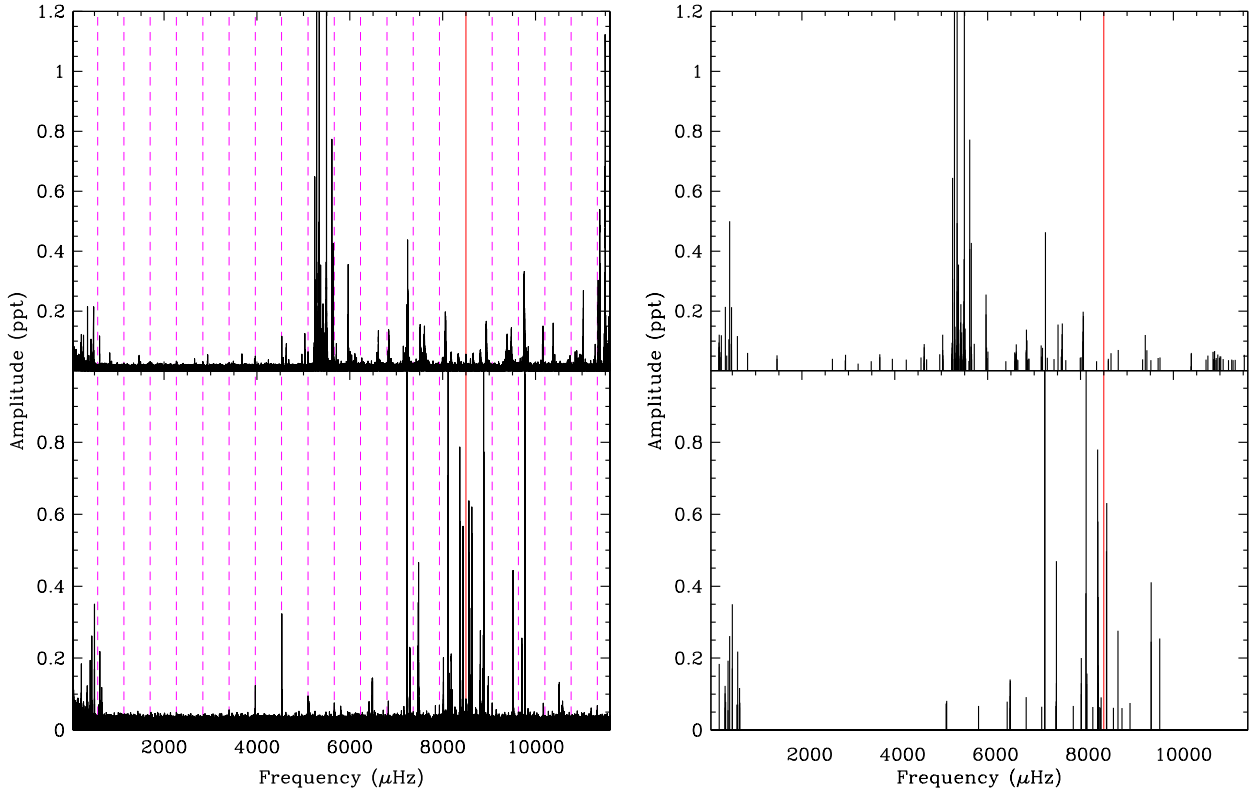

Figure 5. Left-hand panels: Fourier transforms of PG 0048+091 (top) and PG 1315−123 (bottom). FT amplitudes are truncated so lower-amplitude pulsations are visible. Dashed vertical lines indicate known spacecraft artefacts and the solid vertical line indicates the Nyquist frequency. Right-hand panels: schematic representation of FTs where periodicities considered intrinsic to each star are indicated with lines. Only the Nyquist artefact is shown. Note that the bottom axes have no tick marks, so they cannot be confused with low-amplitude pulsations.

4 PG 0048+091 ANALYSES

4.1 Short-period pressure modes

Many of the p-mode frequencies are in multiplets as shown in a ∼300 μHz region in Fig. 8. While these features appear obvious when glancing at the FT, upon closer inspection there are complicating issues. These issues include relatively large frequency splittings in a rich pulsation spectrum, sub- and super-Nyquist frequencies, and uneven frequency splittings. Unlike most other sdB stars, the multiplets in PG 0048+091 have splittings > 2 μHz and because of the pulsation density, sometimes the multiplets overlap, making it more difficult to separate them . Also, as PG 0048+091 has both sub- and super-Nyquist frequencies, reflections of multiplets can overlap intrinsic multiplets, creating complex multiplet regions.

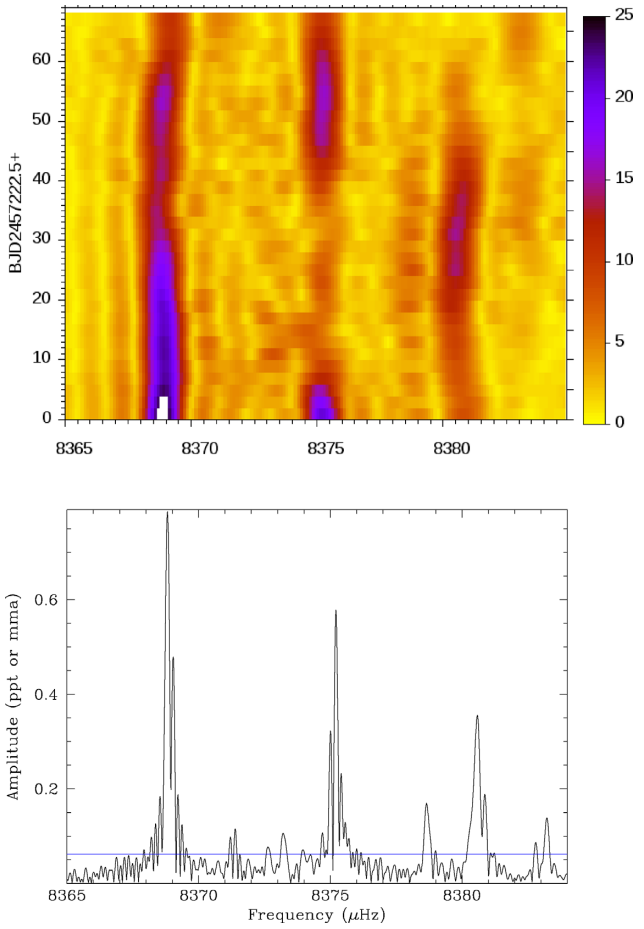

Figure 6. Fouriertransforms for PG 1315−123 showing variable pulsation amplitudes. Top: SFT showing the time evolution of pulsations. Amplitudes are in σ. Bottom: FT of the same region for the entire data set with amplitudes in ppt and the detection limit (4.35σ) indicated with a horizontal line.

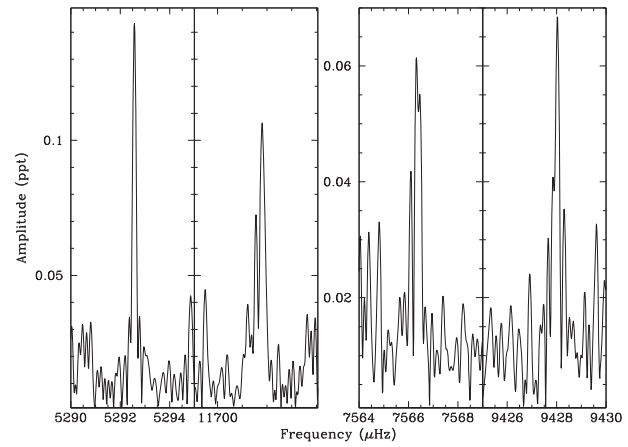

Figure 7. Comparisons of sub- and super-Nyquist regions of PG 0048+091. For the left-hand set, we presume the sub-Nyquist frequency is intrinsic to the star while in the right-hand set, we presume it is the super-Nyquist one.

Likely the most complicating feature is that splittings, while similar, are not the same from multiplet to multiplet and many of the multiplets themselves are not evenly split in frequency. This is most easily shown in Fig. 9 where multiplets are stacked and centred with vertical lines at the average splittings.

In total, we found 24 multiplets, which include 84 frequencies with an average splitting of 2.64 ± 0.31 μHz. The multiplets range from $\ell = 1$ doublets or triplets to an $\ell \geq 4$ nonuplet. In Table 4 we list the minimum degree and the azimuthal order (in ambiguous cases, we presume the highest amplitude to be $m = 0$) with no regard for distance between multiplets that might have the same degree.

In addition to multiplets spaced around 2.64 μHz, there seem to be splittings near 0.43 μHz and integer multiples. These are shown in Fig. 11 with the vertical lines as references for that splitting. It is possible they are created by amplitude and/or phase variations, since we know at least the amplitudes are variable, but it is difficult to explain more than doublets or triplets in that manner. As such, we do not have an explanation for these unusually split multiplets at this time.

4.2 Long-period g-mode analyses

The g-mode analysis is somewhat simpler than the p-mode one simply because there are fewer g-mode periodicities (provided in Table 5). Of the 18 periodicities detected, 9 have close companions indicative of multiplets. However, the frequency splittings are not those commensurate with the dominant p-mode splitting. The top panel of Fig. 12 shows three multiplets on a scale appropriate for the p-mode splitting. One could almost see a doublet appropriate for $\ell = 1$ or an $\ell = 4$ triplet. However, the doublet is 30 per cent too narrow and the possible $\ell = 4$ triplet is commensurate with the asymptotic period spacing, described below. As such, we do not see any multiplets at splittings predicted by the p-mode multiplets. The g-mode multiplets we do find consist of three doublets with splittings of 0.395, 0.901, and 0.405 μHz, and one triplet with splittings of 0.562 and 0.623 μHz. The simplest interpretation of the doublets is splittings with $\Delta m = 1$, 2, and 1. The bottom four panels of Fig. 12 show the multiplets with vertical lines at 0.4, 0.9, and 1.80 μHz. The triplet near 480 μHz is sort of in between. It is too wide for $\ell = 1$ but too narrow for $\ell \geq 2$. It is discussed in the context of asymptotic period spacings.

A successful way to identify pulsation modes in sdBV stars is to detect an asymptotic period sequence. All published *Kepler*-observed g-mode sdBV stars to date show asymptotic period sequences with spacings of about 250 s for $\ell = 1$ and 150 s for $\ell = 2$ (Reed et al. 2011) with the possible exception of the p-mode-dominated KIC 10139564 (Baran et al. 2012). The Kolomogorov–Smirnov (KS) test has proven useful for finding the sequences (Reed et al. 2011) and our result for PG 0048+091 is shown in the left-hand panel of Fig. 13. The deepest trough appears between 200 and 210 s and we generated Echelle diagrams covering those period spacings. Those diagrams, in turn, provided periods that produced a sequence, from which we did a linear-regression fit. The result is a period spacing of 207.45 ± 0.40 s and the Echelle diagram for that is shown in the right-hand panel of Fig. 13 with the fitted periods indicated by black circles. This spacing is peculiarly short if $\ell = 1$ and quite large if $\ell = 2$ for sdBV stars. Of the 13 independent periods, 7 fit the sequence. If we assume the sequence is for $\ell = 1$ (which we will, as explained in Section 4.4), then none of the remaining periods reasonably fit the $\ell = 2$ or 3 sequences, while two (including the triplet) fit the $\ell = 4$ sequence to better

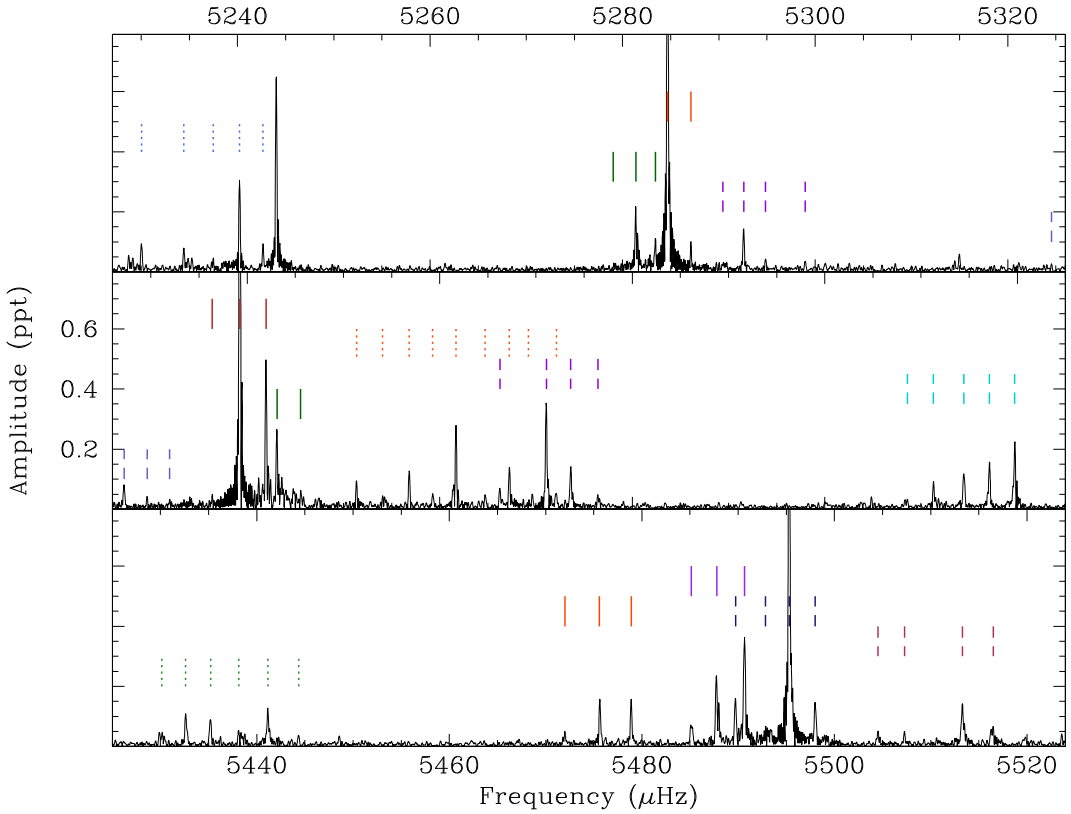

Figure 8. Continuous sections of PG 0048+091's FT showing multiplets with the dominant splitting near 2.6 μHz. Solid, dashed, and dotted lines indicate multiplets with 2–3, 4–5, and >6 members, respectively. Lines are at different levels (and colours on-line) to help distinguish different multiplets.

than 10 per cent. The frequency doublets fit into the $\ell = 1$ asymptotic sequence and their frequency splitting of 0.417 μHz would indicate $\ell = 2$, 3, and 4 multiplet splittings of 0.695, 0.764, and 0.792 μHz, respectively. While the frequency splitting of the triplet deviates by 44 per cent from its expected value based on the $\ell = 1$ splittings, it is the best we can find, and so we cautiously identify them as $\ell = 4$.

4.3 Unusual p modes

While all of the pulsations display amplitude variations that produce some quantity of peak forking (e.g. see Fig. 6), there are regions that are especially complex, creating wide regions of excess pulsation power. Fig. 14 shows two sample regions, in both SFTs and the power spectra of the full data sets with the Lorentzian fits. The SFTs show that amplitudes appear to be changing wildly with frequencies coming and going, and interacting throughout. As each FT within the SFT spans 20 d, the pulsations are likely variable on time-scales much shorter than that. As in Østensen et al. (2014a), we Lorentzian fitted the power spectra (shown in the bottom panels of Fig. 14) with the Lorentzian widths (LW) and power (H_i) provided in Table 6. The Lorentzian widths are inversely proportional to the mode lifetimes (with a proportionality factor related to a turbulent-motion assumption; Østensen et al. 2014a). Some of the regions are difficult to discern as to what should be fitted (6831 and 9395 μHz) and for those we provide two entries in Table 6. The LWs of the four clearest examples (7237, 7517, 8339, and 8656 μHz) average to 6.65 μHz, which results in a mode lifetime of 9.8 h.

4.4 PG 0048+091 discussion

The sdB component of PG 0048+091 is a rare, rich p-mode-dominated hybrid sdBV star, very similar to KIC 10139564. One of the main results of Reed et al. (2007) was the possible detection of stochastic pulsations in PG 0048+091. With this longer-duration, evenly sampled, single-instrument *K2* data set, we can conclude that most of the pulsations in PG 0048+091 are not stochastic in nature. The amplitude variations of most peaks are too small for the variations observed by Reed et al. (2007) and the peak shapes (e.g. Fig. 9) are quite dissimilar to those expected from stochastic oscillations (e.g. Fig. 14). Yet of the 28 frequencies detected in Reed et al. (2007), 7 *do* occur in regions we find to have stochastic properties. The variations observed by Reed et al. (2007) in the other frequencies were almost certainly caused by beating between frequencies in PG 0048+091's rich pulsation spectrum. The mode lifetime we find for the stochastic regions corresponds well with that determined by Reed et al. (2007).

As we have multiplets, we can examine p-mode overtone spacing, which is quite a rare thing. From typical structure models (Charpinet et al. 2000), p-mode overtones are expected to be spaced by 800 to 1100 μHz, independent of degree. Measuring p-mode overtone spacings has only conclusively been done for KIC 10139564 (Baran et al. 2012), where spacings were 3 to 4 times smaller than models predicted. In two other cases, KIC 3527751 (Foster et al. 2015) and Balloon 090100001 (Baran et al. 2009) overtone spacings were measured with much less confidence, but in agreement with model predictions.

PG 0048+091 is another case where we have many p-mode multiplets. As can be seen in Fig. 8, it is not trivial to assign mode

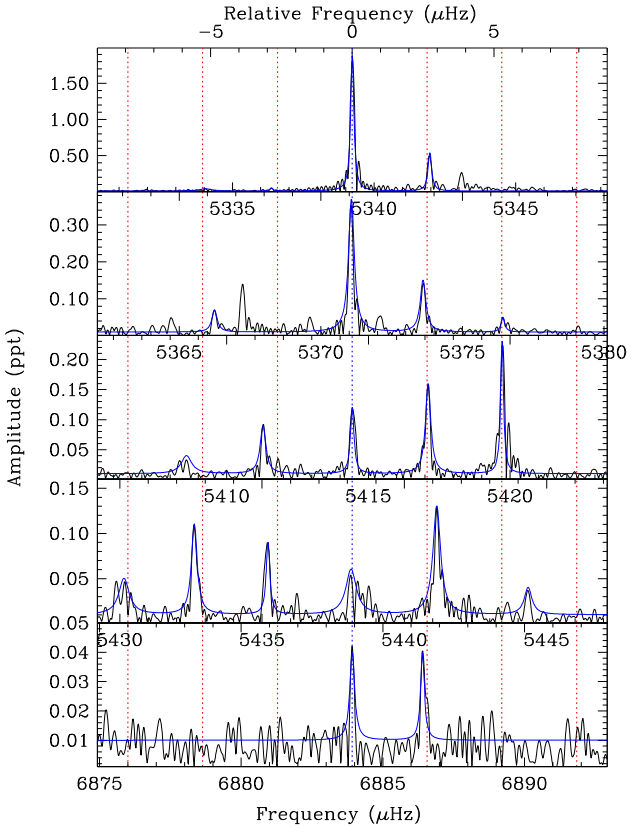

Figure 9. p-mode multiplets in PG 0048+091 stacked to compare frequency splittings. The relative frequency is provided at the top with the central (blue) vertical dashed line indicating the position of the $m = 0$ component. The other (red) vertical lines indicate successive azimuthal values at a spacing of 2.64 μHz. Solid blue lines indicate Lorentzian fits to the frequencies.

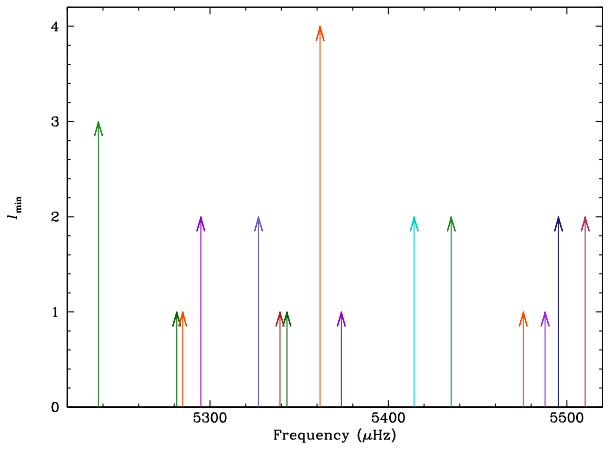

Figure 10. Schematic of p-mode multiplets in PG 0048+091 for the dense region shown in Fig. 8. Each arrow represents the $m = 0$ component of a multiplet.

degrees to the multiplets since most of the multiplets must be incomplete. There are doublets right next to triplets (e.g. f40–f42 and f43–f44, and shown in the top panel of Fig. 8) and neighbouring quintuplets (e.g. f45–f48, f51–f54, and f55–f58) far too close to be consecutive overtones. The densest multiplet region is shown schematically in Fig. 10. The distances between possible $\ell = 1$

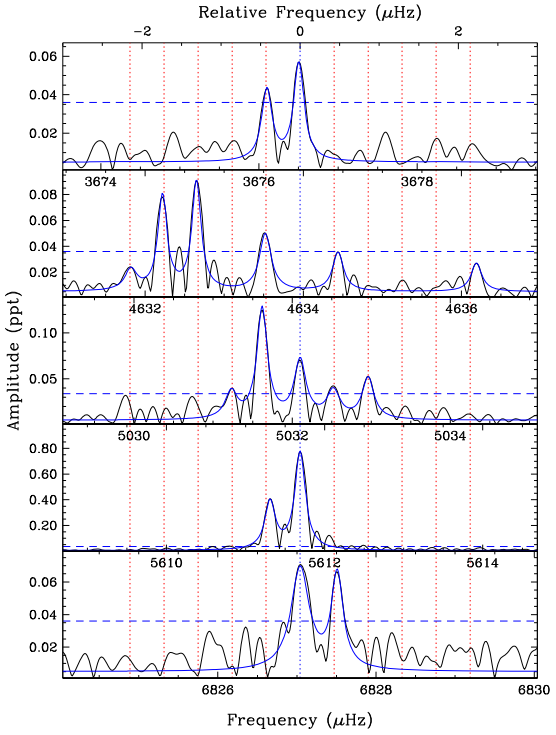

Figure 11. p-mode multiplets in PG 0048+091 with an unusual splitting of 0.43 μHz. The dashed horizontal line is the detection limit.

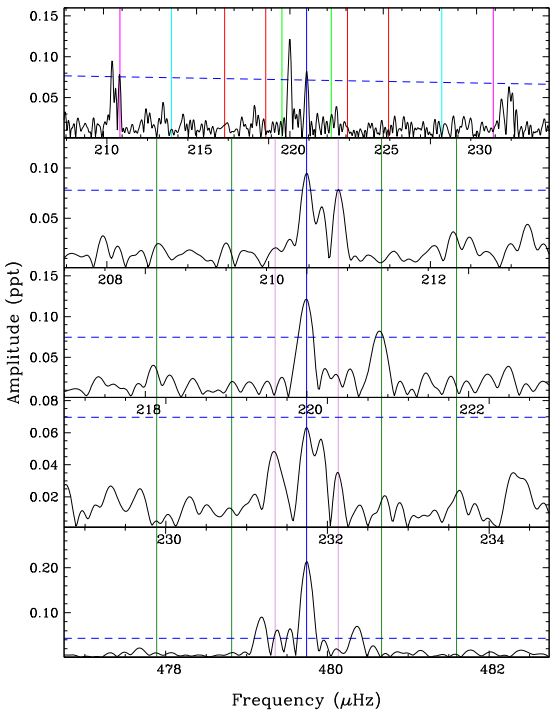

Figure 12. Possible g-mode multiplets in PG 0048+091. Top panel spans 26 μHz with vertical lines indicating splittings, from centre outwards, appropriate for $\ell = 1$ (green, 1.32 μHz), 2 (red, 2.19 μHz), 3 (cyan, 2.42 μHz), and 4 (magenta, 2.50 μHz) for a rotation period of 4.4 d. The remaining panels span 6 μHz with lines for observed splittings of 0.4 and 0.9 μHz. Horizontal dashed (blue) lines indicate the detection limit.

Table 4. p-mode frequencies detected for PG 0048+091. Column 1 provides an ID, column 2 frequencies with errors (Lorentzian widths), column 3 the amplitude, and column 4 the S/N. Column 5 provides a mode identification, if determined, and column 6 lists the closest frequency from Reed et al. (2007). If column 3 says 'stochastic', then there is a a broad excess of power which is described in Section 4.3.

ID	Freq (μHz)	Amp (ppt)	S/N	ℓ, m	$f_{2004/5}$	ID	Freq (μHz)	Amp (ppt)	S/N	ℓ, m	$f_{2004/5}$
f1	1459.17 (0.08)	0.052	6.8			f61	5361.70 (0.06)	0.284	37.1	4,0	
f2	1462.49 (0.08)	0.041	5.4			f62	5364.71 (0.11)	0.052	6.8	4,1	
f3	2652.82 (0.08)	0.041	5.3			f63	5366.25 (0.11)	0.076	9.9	2,−2	
f4	2931.54 (0.07)	0.035	4.6			f64	5367.23 (0.11)	0.130	16.9	4,2	
f5	2935.90 (0.08)	0.054	7.1			f65	5369.23 (0.11)	0.049	6.4	4,3	
f6	3210.12 (0.13)	0.025	3.3			f66	5371.08 (0.12)	0.355	46.4	2,0	
f7	3493.35 (0.10)	0.033	4.3			f67	5372.14 (0.11)	0.062	8.1	4,4	
f8	3676.10 (0.08)	0.046	6.0			f68	5373.61 (0.12)	0.138	18.0	2,1	
f9	3676.51 (0.08)	0.056	7.3			f69	5376.43 (0.08)	0.051	6.7	2,2	
f10	3947.43 (0.07)	0.041	5.4			f70	5404.84 (0.08)	0.042	5.5		
f11	4244.34 (0.07)	0.038	5.0			f71	5408.58 (0.22)	0.049	6.4	2,−2	5407.0
f12	4564.93 (0.07)	0.045	5.9			f72	5411.28 (0.12)	0.092	12.0	2,−1	
f13	4631.82 (0.09)	0.026	3.4			f73	5414.43 (0.08)	0.114	14.9	2,0	
f14	4632.22 (0.07)	0.079	10.3			f74	5417.11 (0.11)	0.162	21.1	2,1	
f15	4632.65 (0.07)	0.090	11.8	2,−2		f75	5419.72 (0.06)	0.223	29.2	2,2	
f16	4633.52 (0.09)	0.049	6.4	2,−1		f76	5430.15 (0.22)	0.050	6.5	3,−2	
f17	4634.44 (0.08)	0.036	4.7	2,0		f77	5432.62 (0.12)	0.109	14.2	3,−1	
f18	4636.19 (0.08)	0.028	3.6	2,2		f78	5435.21 (0.08)	0.092	12.1	3,0	
f19	4681.77 (0.08)	0.039	5.1			f79	5438.13 (0.22)	0.057	7.4	3,1	
f20	4964.39 (0.08)	0.056	7.3			f80	5441.14 (0.16)	0.129	16.8	3,2	
f21	5028.06 (0.09)	0.033	4.3			f81	5444.35 (0.16)	0.041	5.4	3,3	
f22	5031.23 (0.09)	0.039	5.1			f82	5448.57 (0.09)	0.036	4.7		
f23	5031.62 (0.08)	0.121	15.8			f83	5472.00 (0.22)	0.050	6.5	1,−1	5465.1
f24	5032.10 (0.09)	0.070	9.1			f84	5475.59 (0.12)	0.158	20.6	1,0	
f25	5032.52 (0.10)	0.040	5.2			f85	5478.90 (0.08)	0.158	20.7	1,1	
f26	5032.96 (0.09)	0.052	6.8			f86	5485.13 (0.22)	0.071	9.3	1,−1	
f27	5228.70 (0.09)	0.058	7.6		5203.1	f87	5487.80 (0.12)	0.233	30.5	1,0	5487.2
f28	5229.14 (0.08)	0.045	5.9			f88	5489.73 (0.12)	0.163	21.4	2,−2	
f29	5230.04 (0.12)	0.094	12.3	3,−3		f89	5490.66 (0.08)	0.373	48.7	1,1	
f30	5234.43 (0.10)	0.078	10.2	3,−1		f90	5492.85 (0.32)	0.062	8.1	2,−1	
f31	5235.28 (0.07)	0.051	6.6			f91	5495.30 (0.08)	1.576	205.9	2,0	
f32	5237.49 (0.08)	0.041	5.4	3,0		f92	5498.00 (0.11)	0.148	19.3	2,1	
f33	5240.21 (0.11)	0.308	40.3	3, +1		f93	5504.54 (0.15)	0.063	8.2	2,−2	
f34	5242.65 (0.06)	0.091	11.9	3, +2		f94	5507.29 (0.08)	0.050	6.6	2,−1	
f35	5244.03 (0.07)	0.644	84.2		5244.9	f95	5513.30 (0.12)	0.142	18.6	2,1	
f36	5279.03 (0.10)	0.040	5.2	1,−1		f96	5516.49 (0.15)	0.071	9.3	2,2	
f37	5281.37 (0.07)	0.229	29.9	1,0		f97	5523.61 (0.08)	0.042	5.5		
f38	5283.42 (0.08)	0.101	13.2	1,1		f98	5594.99 (0.08)	0.034	4.4		
f39	5284.66 (0.13)	1.607	210.0	1,0		f99	5611.31 (0.08)	0.407	53.2		
f40	5287.10 (0.06)	0.106	13.9	1,1	5287.6	f100	5611.69 (0.08)	0.772	100.8		5612.2
f41	5290.42 (0.66)	0.040	5.2	2,−2		f101	5642.84 (0.10)	0.082	10.7	2,−1	
f42	5292.59 (0.07)	0.148	19.4	2,−1		f102	5645.59 (0.08)	0.080	10.4	2,0	
f43	5294.85 (0.08)	0.043	5.6	2,0		f103	5647.55 (0.09)	0.427	55.8		
f44	5298.97 (0.11)	0.041	5.4	2,2		f104	5649.41 (0.08)	0.039	5.1		
f45	5314.52 (0.08)	0.037	4.8			f105	5651.25 (0.12)	0.057	7.4	2,2	5652.9
f46	5314.96 (0.08)	0.061	8.0			f106	5710.12 (0.19)	0.091	11.9		
f47	5324.56 (0.06)	0.027	3.6	2,−1		f107	5963.77 (0.12)	0.189	24.7	1,-1	
f48	5327.21 (0.07)	0.086	11.2	2,0		f108	5965.63 (0.10)	0.255	33.3	1,0	
f49	5329.61 (0.08)	0.042	5.5	2,1		f109	5975.03 (0.09)	0.078	10.1		
f50	5331.95 (0.11)	0.030	3.9	2,2		f110	5988.34 (0.09)	0.043	5.6		
f51	5334.05 (0.26)	0.042	5.4			f111	6002.02 (0.08)	0.065	8.5		
f52	5336.38 (0.06)	0.049	6.4	1,−1		f112	6388.90 (0.09)	0.033	4.3		
f53	5339.23 (0.07)	1.792	234.2	1,0		f113	6582.64 (0.09)	0.062	8.1	1,0	
f54	5341.97 (0.08)	0.493	64.4	1,1		f114	6586.22 (0.08)	0.033	4.4	1,1	
f55	5343.10 (0.06)	0.266	34.8	1,0		f115	6595.04 (0.20)	0.039	5.1	2,−1	
f56	5345.56 (0.17)	0.073	9.5	1,1		f116	6597.79 (0.08)	0.034	4.4	2,0	
f57	5351.36 (0.06)	0.096	12.6	4,−4		f117	6602.89 (0.12)	0.058	7.6	2,2	
f58	5354.07 (0.07)	0.045	5.9	4,−3		f118	6605.36 (0.14)	0.037	4.8		

Table 4 – *continued*

ID	Freq (μHz)	Amp (ppt)	S/N	ℓ, m	$f_{2004/5}$	ID	Freq (μHz)	Amp (ppt)	S/N	ℓ, m	$f_{2004/5}$
f59	5356.84 (0.08)	0.129	16.9	4,−2	5356.9	f119	6607.59 (0.07)	0.040	5.2		
f120	6608.54 (0.07)	0.045	5.9			f157	8059.34 (0.12)	0.184	24.0	1	
f121	6609.66 (0.10)	0.052	6.8	1,−1	6609.2	f158	8061.50 (0.09)	0.176	23.0		
f122	6611.93 (0.08)	0.065	8.4	1,0		f159	8341.80 (stochastic)	0.033	4.3		
f123	6613.10 (0.12)	0.059	7.7				8497.16	Nyquist			
f124	6614.27 (0.12)	0.089	11.6	1,1		f160	8598.27 (0.09)	0.041	5.4		
f125	6622.89 (0.09)	0.038	5.0	2,−1		f161	8599.65 (0.08)	0.035	4.6		
f126	6624.87 (0.08)	0.040	5.2	2,0		f162	8653.61 (stoc)				8651.4
f127	6628.67 (0.09)	0.036	4.7	2,2		f163	8811.42 (stoc)				8820.6
f128	6648.51 (0.09)	0.036	4.7			f164	9334.26 (0.08)	0.039	5.1		9352.8
f129	6827.04 (0.14)	0.069	9.0			f165	9395.46 (stoc)				9385.3
f130	6827.51 (0.09)	0.062	8.1			f166	9427.99 (0.19)	0.069	9.0		
f131	6832.16	(stoc)			6834.3	f167	9513.38 (0.12)	0.036	4.7		
f132	6839.97 (0.08)	0.041	5.4			f168	9666.40 (0.10)	0.043	5.6		
f133	6845.70 (0.08)	0.102	13.3			f169	9711.76 (0.08)	0.045	5.9		9694.6/9795.1
f134	6858.87 (0.10)	0.037	4.8			f170	10377.75 (0.10)	0.016	2.1	−1	10366.8
f135	6883.92 (0.10)	0.042	5.5	1,0		f171	10382.71 (0.12)	0.057	7.5	1	
f136	6886.40 (0.08)	0.040	5.3	1,1		f172	10385.12 (0.15)	0.060	7.8	2	
f137	7150.54 (0.09)	0.085	11.1			f173	10700.67 (0.10)	0.038	5.0		
f138	7158.03 (0.08)	0.048	6.3		7154.3	f174	10739.29 (0.10)	0.051	6.7		
f139	7165.52 (0.08)	0.048	6.3			f175	10849.70 (0.15)	0.064	8.4		
f140	7177.00	(stoc)				f176	10862.52 (0.09)	0.040	5.2		
f141	7240.79	(stoc)			7237.0	f177	10878.54 (0.10)	0.064	8.4	−1	
f142	7282.36 (0.08)	0.044	5.8			f178	10884.20 (0.08)	0.067	8.8	1	
f143	7428.99 (0.09)	0.040	5.2		7430.1	f179	10916.73 (0.09)	0.037	4.8		
f144	7514.57	(stoc)			7501.3/7523.9	f180	10918.04 (0.08)	0.043	5.6		
f145	7585.10 (0.08)	0.048	6.2		7560.0	f181	10954.97 (0.16)	0.055	7.2		
f146	7594.71 (0.09)	0.073	9.6			f182	10988.91 (0.10)	0.043	5.6		
f147	7598.80 (0.08)	0.123	16.1			f183	10998.18 (0.11)	0.049	6.4		
f148	7605.73 (0.08)	0.159	20.7		7610.1	f184	11019.93 (0.10)	0.049	6.4		
f149	7679.60 (0.13)	0.036	4.7			f185	11071.76 (0.11)	0.040	5.2		11103.3
f150	7993.86 (0.09)	0.044	5.7			f186	11182.39 (0.11)	0.036	4.7		11159.8
f151	8008.49 (0.09)	0.046	6.0			f187	11252.21 (0.09)	0.038	5.0		
f152	8049.90 (0.20)	0.099	12.9	1,−1		f188	11280.36 (0.18)	0.036	4.7		
f153	8054.06 (0.08)	0.132	17.2	1,−1		f189	11327.48 (0.11)	0.037	4.8		
f154	8054.95 (0.08)	0.131	17.1	1,1	8055.5	f190	11522.33 (0.08)	0.054	7.1		
f156	8054.71 (0.08)	0.198	25.9	1,0							

multiplets are 3, 58, 31, 102, 12, 1124, 272, 1169, 4, and 2825 μHz, respectively, rounded to the nearest integer. Possible $\ell = 2$ multiplets are spaced by 32, 12, 75, 21, 60, 15, 135, 952, and 3782 μHz and the $\ell = 3$ multiplets are separated by 198 μHz. The density of multiplets is clearly a problem. In just the 300 μHz-wide region shown in Fig. 10, there are portions of at least 15 separate multiplets. If we presume two multiplets per degree, this would correspond to overtone spacings of ∼200 μHz and require $\ell = 7$ pulsations. Such high-degree modes are unlikely because of geometric cancellation (Pesnell 1985), particularly since this region includes some of the highest-amplitude pulsations of PG 0048+091. As such, we have to conclude that PG 0048+091 has p-mode overtone spacings that are likely similar to KIC 10139564 and much smaller than model predictions.

As we have both p- and g-mode pulsations with multiplets, we can compare their splittings with regard to rotation. p-mode pulsations predominantly sample the envelope while g modes probe deeper, down to the convective core (Charpinet et al. 2014). While there is significant overlap, we will consider p modes as measuring the rotation in the envelope and g modes as measuring the rotation near to the core (below the He/H transition). The best p-mode multiplets average to 2.64 ± 0.31 μHz, which would give a spin period of 4.38 ± 0.40 d, using $C_{n,\ell} = 0$. There are no corresponding g-mode multiplet splittings. Our best estimate is that there are three $\ell = 1$ multiplets with an average splitting of 0.417 ± 0.030 μHz, which would indicate a spin period of 13.88 ± 0.92 d. This means that the envelope is spinning just over 3 times faster than the stellar interior. We also have to mention the smaller split p-mode multiplets (Fig. 11). Their splitting (∼0.43 μHz) is very similar to that observed in the g-mode multiplets (0.417 μHz), making it possible that all of these splittings are caused by amplitude variations on a common time-scale. Such a common time-scale could point to variations within the driving region, but that is beyond the scope of this paper. If all of the multiplets near 0.4 μHz are caused by something other than rotation, then the g-mode rotation period must be longer than can be measured with this data set: approximately >45 d. In this paper, we infer that the g-mode splittings *are* caused by rotation while we do not know the cause of the ∼0.43 μHz p-mode splittings.

The inferred ratio of core/envelope rotation is amazingly similar to the only other hybrid pulsator where multiplets were observed in both the p- and g-mode regions (Foster et al. 2015). KIC 3527751 was shown to be predominantly a g-mode pulsator, with some p-mode multiplets, which were used to deduce core/envelope rota-

Table 5. g-mode frequencies detected for PG 0048+091. Column 1 provides an ID; columns 2 and 3 provide frequencies and periods with errors (Lorentzian widths) in parentheses. Column 4 lists the amplitude and column 5 lists the corresponding S/N. Column 6 lists the mode degree and azimuthal order, if a multiplet. Column 7 lists the relative radial indices and column 8 the deviation from the asymptotic sequence.

ID	Freq (μHz)	Period (s)	Amp (ppt)	S/N	ℓ, m	n	$\delta P/\Delta\Pi$ per cent
fA	210.470 (0.083)	4751.27 (1.86)	0.095	5.3	1,0	22	4.6
fB	210.865 (0.061)	4742.37 (1.37)	0.079	4.4	1,1	22	0.3
fC	218.088 (0.052)	4585.31 (1.10)	0.052	4.9	4,–	69	3.8
fD	219.996 (0.094)	4545.54 (1.95)	0.121	11.4	1,−1	21	5.4
fE	220.897 (0.105)	4527.00 (2.15)	0.082	7.8	1,1	21	−3.5
fF	231.337 (0.087)	4322.70 (1.62)	0.048	4.6	1,−1	20	−2.0
fG	231.742 (0.082)	4315.14 (1.53)	0.063	6.0	1,0	20	−5.7
fH	236.182 (0.079)	4234.02 (1.41)	0.046	4.3			
fI	264.854 (0.071)	3775.67 (1.02)	0.119	11.2			
fJ	348.079 (0.071)	2872.91 (0.59)	0.214	21.4	1,–	13	−0.9
fK	378.662 (0.068)	2640.88 (0.47)	0.051	5.1			
fL	426.756 (0.066)	2343.26 (0.36)	0.106	10.0			
fM	443.703 (0.080)	2253.76 (0.40)	0.500	47.0	1,–	10	0.7
fN	479.181 (0.059)	2086.89 (0.26)	0.091	8.5	4,−1	31	−4.6
fO	479.743 (0.071)	2084.45 (0.31)	0.213	20.1	4,0	31	−8.3
fP	480.366 (0.060)	2081.75 (0.26)	0.070	6.6	4,1	31	−12.5
fQ	610.678 (0.072)	1637.52 (0.19)	0.117	11.0	1,–	7	3.6
fR	826.394 (0.067)	1210.08 (0.10)	0.060	5.7	1,–	5	−2.4

Table 6. Lorentzian widths and power (H_i) fitted to observations for PG 0048+091.

Freq (μHz)	LW (μHz)	H_i (ppt^2)	Freq (μHz)	LW (μHz)	H_i (ppt^2)
6831	0.5/2.0	6.2/3.9	8339	7.0	0.6
7175	10.4	0.5	8656	6.9	0.6
7237	6.7	12.6	8812	2.5	1.1
7517	5.6	3.4	9395	3.7/15.9	4.2/1.9

tion periods of 42.6 ± 3.4/15.3 ± 0.7 d (Foster et al. 2015). While the spin periods of PG 0048+091 are much shorter (the fastest *Kepler*-observed rotator observed so far), it is worth noting how similar the ratio is, 3.3 for PG 0048+091 and 2.8 for KIC 3527751. Another star, EPIC 211779126, was also presumed to have a slower-rotating core than envelope (Baran et al. 2017). In that case, p-mode multiplets were observed indicating a rotation period of 16 d, but no g-mode multiplets were observed, indicating a core rotation period longer than about 40 d.

PG 0048+091 is also the first time where we have an sdB + MS binary with rotation periods for both components. The measured $v_r \sin i$ of $26^{+2.0}_{-1.6}$ km s^{-1} gives a rotation period of roughly 2–3 d for the F component. This is not dissimilar to the envelope rotation period of the sdB star, at 4.4 d. We note that the measured $v_r \sin i$ of the companion is comparable to those in Vos et al. (2018) for sdB + F–K binaries.

While far fewer, the g modes are still useful for detecting an asymptotic sequence. We find that PG 0048+091 has the shortest period spacing yet detected for sdBV stars at 207.45 ± 0.40 s. This is an interesting match with KIC 10139564 (Baran et al. 2012), which could have an $\ell = 1$ sequence at 207 or 310 s, assuming it is 207 s. As both of these stars are predominantly p-mode pulsators, with similar $T_{\rm eff}$, and $\log g$, their overtone spacing could be the first connection between pulsators at the hot end of the extreme horizontal branch.

PG1315 1315−123 ANALYSES

5.1 Short-period pressure-mode analyses

As can be seen in Fig. 5 the main power in the p-mode pulsation spectrum of PG 1315−123 is at high frequency, the highest of any *Kepler*-observed sdBV star so far. And the pulsation spectrum has similar complications as PG 0048+091 in that there are super-Nyquist frequencies, multiplets of varying sizes, and regions with broad regions of excess power indicative of stochastic pulsations. Table 8 lists the 46 p-mode frequencies we consider to be intrinsic to PG 1315−123. There are three nice multiplets (shown in the top panels of Fig. 15), a doublet (f13, f14), a triplet (f20–f22), and four of a quintuplet (f6–f9). We use those to determine a frequency splitting of 0.731 ± 0.009 μHz. There are four more possible multiplets and we include those mode identifications in Table 8 and show three of them in the bottom panels of Fig. 15. Two of the multiplets have Nyquist reflections very close to one another. If viewed without considering Nyquist reflections, each appears as a quintuplet, but when amplitude and peak shape are considered, three are sub-Nyquist (f16–f18) and two are super-Nyquist (f44–f45), and that is how we list them.

There is an interesting region that, again, *looks* like a multiplet but upon close inspection seems not to be. The region is shown in Fig. 6 and has three high-amplitude pulsations (f28, f31, and f33) and four low-amplitude ones (f29, f30, f32, and f34). It is tempting to consider the high-amplitude frequencies as a triplet, but the splittings between them are uneven at 6.37 and 5.42 μHz and dissimilar to the determined splitting of 0.71 μHz. The next step would be to consider all seven frequencies as a multiplet, but the splittings between them are also uneven at 2.48, 1.90, 1.99, 3.43, 1.99, and 2.60 μHz. Those also do not match the determined splitting. One can then play mathematical games with the splittings to make them close to the 0.71 μHz. Dividing the splittings by 3, 2, 2, 4, 2, and 3 makes splittings of 0.83, 0.95, 0.99, 0.86, 0.99, and 0.87 μHz, respectively, which would make this multiplet $\ell \geq$

Table 7. p-mode frequencies detected for PG 1315−123. Column 1 provides an ID, column 2 frequencies with errors (Lorentzian widths), column 3 the amplitude, and column 4 the S/N. Column 5 provides a mode identification, if determined. If column 3 says 'stochastic', then there is a 'hump' of power, which is described in Section 5.3.

ID	Freq (μHz)	Amp (ppt)	S/N	ℓ, m	ID	Freq (μHz)	Amp (ppt)	S/N	ℓ, m
f1	5106.67 (0.08)	0.073	5.10		f24	8116.05 (0.09)	1.79	125.17	
f2	5111.49 (0.08)	0.076	5.31	−1	f25	8127.44 (0.1)	0.128	8.95	
f3	5113.48 (0.09)	0.081	5.66	1	f26	8136.18 (0.087)	0.157	10.98	
f4	5799.86 (0.09)	0.067	4.69		f27	8264.29 (0.11)	0.064	4.48	
f5	6418.1	stochastic	–		f28	8368.85 (0.18)	0.78	54.55	
f6	6482.81 (0.09)	0.095	6.64	−2	f29	8371.33 (0.2)	0.11	7.69	
f7	6483.55 (0.08)	0.061	4.27	−1	f30	8373.23 (0.1)	0.11	7.69	
f8	6484.3 (0.09)	0.141	9.86	0	f31	8375.22 (0.19)	0.58	40.56	
f9	6485.03 (0.08)	0.13	9.09	1	f32	8378.65 (0.11)	0.18	12.59	
f10	6485.41 (0.09)	0.137	9.58		f33	8380.64 (0.22)	0.37	25.87	
f11	6828.25 (0.08)	0.092	6.43		f34	8383.24 (0.13)	0.13	9.09	
f12	7159.52 (0.09)	0.065	4.55		f35	8414.01 (0.08)	0.064	4.48	
f13	7226.85 (0.09)	1.11	77.62	−1	f36	8424.49 (0.08)	0.061	4.27	
f14	7228.23 (0.09)	1.29	90.21	1	f37	8440.49 (0.08)	0.091	6.36	
f15	7467.14 (0.09)	0.067	4.69		f38	8557.69 (0.28)	0.497	34.76	−2
f16	7475.24 (0.09)	0.08	5.59	−2	f39	8560.09 (0.15)	0.631	44.13	1
f17	7476.74 (0.39)	0.13	9.09	0	f40	8707.68 (0.09)	0.062	4.34	
f18	7477.95 (0.12)	0.47	32.87	2	f41	8804.09	stochastic		
f19	7842.21 (0.1)	0.067	4.69		f42	8893.17 (0.09)	0.061	4.27	
f20	8013.78 (0.09)	0.2	13.99	−2	f43	9063.62 (0.09)	0.075	5.24	
f21	8015.34 (0.09)	0.1	6.99	0	f44	9520.13 (0.21)	0.246	17.20	−1
f22	8016.87 (0.1)	0.13	9.09	2	f45	9521.23 (0.18)	0.411	28.74	0
f23	8114.48	stochastic			f46	9706.1	stochastic		

Table 8. g-mode frequencies detected for PG 1315−123. Column 1 provides an ID; columns 2 and 3 provide frequencies and periods with errors (Lorentzian widths) in parentheses. Column 4 lists the amplitude and column 5 lists the corresponding S/N. All identified modes are presumed to be $\ell = 1$ with column 6 listing the azimuthal order, if a multiplet, column 7 listing the relative radial index, and column 8 the deviation from the $\ell = 1$ asymptotic sequence.

ID	Freq (μHz)	Period (s)	Amp (ppt)	S/N	m	n	$\delta P/\Delta\Pi$ per cent
fA	217.289 (0.082)	4602.2 (1.7)	0.184	9.2		23	6.8
fB	345.709 (0.060)	2892.6 (0.5)	0.063	3.5	1		
fC	346.056 (0.080)	2889.7 (0.7)	0.123	6.8	0		
fD	346.394 (0.070)	2886.9 (0.6)	0.102	5.7	−1		
fE	355.050 (0.090)	2816.5 (0.7)	0.078	1.1			
fF	406.265 (0.090)	2461.4 (0.5)	0.055	3.4	1	14	− 1.4
fG	406.618 (0.081)	2459.3 (0.5)	0.193	12.1	0	14	− 2.3
fH	444.046 (0.066)	2252.0 (0.3)	0.261	16.3		13	9.8
fI	497.620 (0.068)	2009.6 (0.3)	0.35	21.9	0	12	6.9
fJ	497.981 (0.080)	2008.1 (0.3)	0.171	10.7	−1	12	6.3
fK	598.057 (0.088)	1672.1 (0.2)	0.071	4.4			
fL	613.987 (0.073)	1628.7 (0.2)	0.218	14.2	0		
fM	614.361 (0.070)	1627.7 (0.2)	0.071	4.6	−1		
fN	656.673 (0.083)	1522.8 (0.2)	0.117	7.6	1	10	0.4
fO	657.417 (0.070)	1521.1 (0.2)	0.063	4.1	−1	10	− 0.3
fP	658.854 (0.075)	1517.8 (0.2)	0.076	4.9			

8. This is ridiculously high and would give the high-amplitude frequencies uneven azimuthal orders of −8, 1, and 5, which is very unlikely. But one can go further and divide the splittings by 4, 3, 3, 5, 3, and 4, respectively, making this an $\ell \geq 11$ multiplet. Again, geometric cancellation makes this very unlikely and would again make the high-amplitude frequencies have uneven azimuthal orders of −11, −1, and 7. After this lengthy math exercise, we are left with a region of unevenly spaced peaks that we cannot assign mode identifications to, even though three of them have quite high amplitudes.

There are four regions of messy power that are indicative of stochastic pulsations. These will be discussed in Section 5.3.

5.2 Long-period g-mode analyses

We detected 13 g-mode periodicities above the 4.35σ detection limit of which 8 are in multiplets. The p-mode frequency splitting of 0.71 μHz would correspond with g-mode frequency splittings of 0.36, 0.59, and 0.65 μHz for $\ell = 1$, 2, and 3, respectively, using $C_{n,\ell} = 1/(\ell + 1)$. Three of the multiplet splittings fit the $\ell = 1$

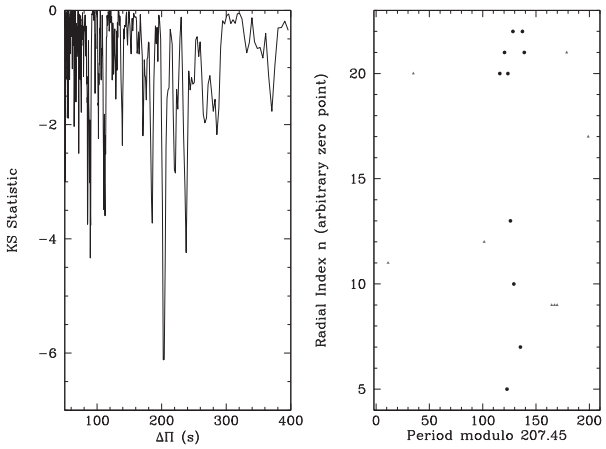

Figure 13. Asymptotic g-mode period spacing for PG 0048+091. Left-hand panel: Kolomogorov–Smirnov test. Right-hand panel: Echelle diagram showing the $\ell = 1$ asymptotic sequence periods with (black) circles and those that are not $\ell = 1$ modes with (red) triangles.

splitting, and upon inspection, there are three more splittings involving peaks that are below 4.35σ. We include those three frequencies in Table 8, even though they are below 4.35σ. Altogether, there are five multiplets we assign as $\ell = 1$ with an average splitting of 0.358 ± 0.014 μHz. These are shown in Fig. 16.

There are 10 independent periods and we use them to search for an asymptotic period sequence. The left-hand panel of Fig. 17 shows results of a KS test that does not reveal any substantial troughs. However, differencing the independent periods reveals spacings near 205 and 240 s. We investigated those by producing Echelle diagrams and calculating linear regressions on various spacings. The best solution we can find is for an $\ell = 1$ period spacing of 236.5 ± 1.3 s and that Echelle diagram is shown in the right-hand panel of Fig. 17. This solution is not wholly satisfactory as it misses two of the five $\ell = 1$ multiplets. It is possible the multiplets that do not fit the asymptotic sequence are trapped modes, but there are too few periodicities to make that sort of a conclusion.

5.3 Unusual p modes

As in Section 4.3 for PG 0048+091 , PG 1315−123 has regions that appear to have stochastic properties. These are shown in Fig. 18 with the fitted Lorentzian widths and power provided in Table 9. The average LW is 3.4 μHz, which corresponds to mode lifetimes of 18.6 h.

5.4 PG 1315−123 discussion

PG 1315−123 is the third *p*-mode-dominated hybrid observed by the *Kepler* space telescope. It is the hottest of the three and most of the pulsation power is at the shortest periods of the three, making it a very interesting object. The real surprise is that it pulsates with g modes at such a high temperature.

While not as rich as PG 0048+091 , we still detect pulsation multiplets in both the p- and g-mode regions, from which we can constrain core/envelope rotation periods. The p-mode multiplets, with a value of 0.731 ± 0.009 μHz assuming $C_{n,\ell} = 0$, indicate a spin period of 15.83 ± 0.19 d and the g-mode multiplets, with a frequency splitting of 0.358 ± 0.014 μHz and assuming they are $\ell = 1$ with $C_{n,\ell} = 0.5$, would have a spin period of 16.18 ± 0.57 d, in good agreement. This indicates that PG 1315−123 rotates as though it were a solid body.

We can also examine p-mode overtones using the multiplets in PG 1315−123. We have identified three $\ell = 1$ and four $\ell = 2$ multiplets. The $\ell = 1$ multiplets are separated by 2115 and 2294 μHz, which likely makes their separations $\Delta n = 2$. The $\ell = 2$ multiplets are separated by 992, 539, and 544 μHz. A separation of 992 μHz is perfectly acceptable for $\Delta n = 1$, but 540 μHz is about half that models predict between overtones. If f20–f22 were $\ell \geq 3$, then the spacings would also fit $\Delta n = 1$. However, with no additional information, we cannot ascertain with certainty if the $\ell = 2$ overtones are $\Delta n = 2$, 1, and 1 with an overtone spacing near 540 μHz or two $\Delta n = 1$ spacings of 990 μHz with an $\ell \geq 3$ multiplet in between.

6 CONCLUSIONS

We have obtained new series of low- and high-resolution spectra of PG 0048+091 and PG 1315−123, the latter only in low resolution. From spectral decomposition we find that in both objects a hot sdB star is accompanied by a late-F main-sequence star, and that the individual components of these binaries have approximately equal flux contributions at 5400 Å. For both binaries the orbital period is likely longer than one year.

The radial velocities of PG 0048+091 prove that the sdB and F star are gravitationally bound. From the spectral types of the main-sequence companions, both late F, we conclude that the observed pulsations are not of δ Scuti type (see Bowman & Kurtz 2018 for a review of δ Scuti pulsations), but must find their origin in the sdB stars. A similar conclusion is based on the observed $v \sin i$ constraint on the rotation period of the F star in PG 0048+091, which likely has a shorter rotation period than the sdB star's interior, where g modes propagate.

We have also constrained rotation for both components of an sdB + MS star for the first time. We have spectroscopically constrained $v \sin i$ for the F component of PG 0048+091 and asteroseismically determined the rotation period for the sdB component. Vos et al. (2018) compared binary periods to rotation velocities for the main-sequence components of nine sdB + F–K binaries. From those, they determined that the mass loss of the sdB progenitor contributed very little to the mass of the MS companion and could occur on time-scales as short as a decade (see their table 8). Such studies should go a long way to understanding the enigmatic process(es) of producing sdB stars from red giant progenitors. Having full dynamic measures of the binary and rotation properties of both stars should provide additional constraints on the mass-transfer/loss mechanisms.

With *K2* data, we have discovered only the second and third examples of *p*-mode-dominated hybrid sdBV stars. And like KIC 10139564, these also have multiplets in both regions, allowing us to examine radially differential rotation and compare radial overtones in both regions.

This makes for some interesting comparisons:

(i) KIC 10139564 and PG 1315−123 rotate as though solid bodies while PG 0048+091 does not, with the envelope rotating faster.

(ii) KIC 10139564, PG 0048+091, and PG 1315−123 are relatively fast rotators. PG 0048+091 has the shortest envelope rotation period (4.4 d) yet observed by *Kepler*. This is interesting since both PG 0048+091 and PG 1315−123 are in long-period (P> 100 d) binaries. Other sdBV stars in short-period (P < 20 d and even

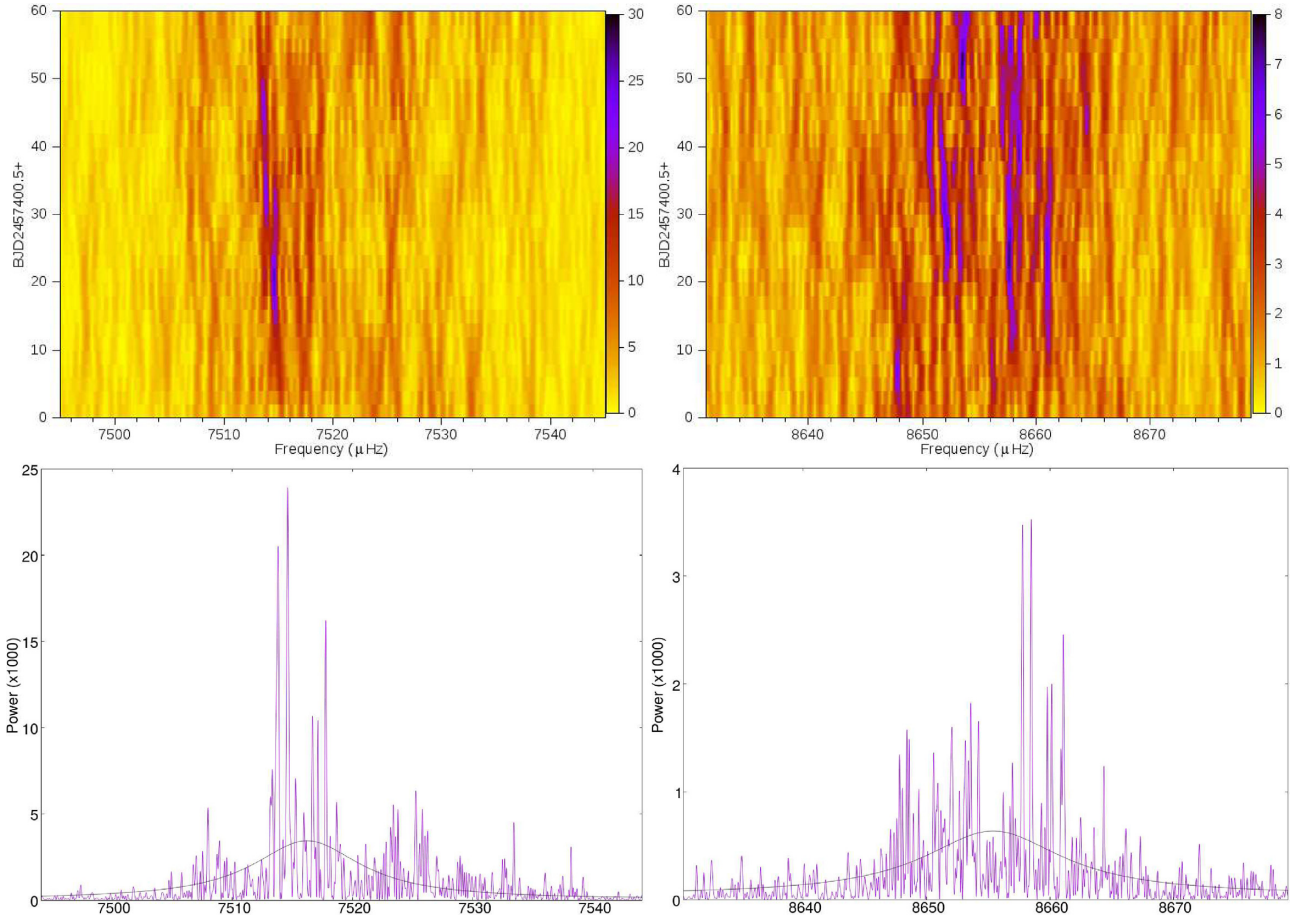

Figure 14. Fourier transforms showing two regionswith stochastic pulsation properties for PG 0048+091. The SFT is like the top panel of Fig. 6. The bottom panel shows the power spectrum with the Lorentzian fit (black line).

down to 0.5 d) binaries rotate subsynchronously with rotation periods longer than PG 0048+091 (summary in Table 1 of Reed et al. 2018b).

(iii) KIC 10139564 and PG 0048+091 have the smallest asymptotic g-mode period spacings at 207 s. While PG 1315−123 is hotter, its asymptotic g-mode period spacings are similar to those measured in g-mode-dominated pulsators. We suspect the shorter periods are related to more compact cores which could be produced by higher-mass progenitors. Evolutionary structural models would be useful for exploring this possibility, but that is beyond the scope of this paper.

(iv) KIC 10139564 and PG 0048+091 have *p*-mode overtone spacings much smaller than predicted by models. The $\ell = 1$ overtone spacing in PG 1315−123 is commensurate with models while the $\ell = 2$ overtones may be just slightly overdense.

(v) With one exception (the predominantly *g*-mode hybrid pulsator KIC 3527751), KIC 10139564, PG 0048+091, and PG 1315−123 are the *only* sdBV stars with detected multiplets in both p- and g-mode regions.

(vi) KIC 10139564 and PG 0048+091 have nearly identical $T_{\rm eff}$ and log *g* while PG 1315−123 is hotter. PG 1315−123 is the hottest *Kepler*-observed sdBV star to date.

(vii) PG 0048+091 and PG 1315−123 are in long-period (P > 100 d) spectroscopic binaries with main-sequence F companions while KIC 10139564 is apparently single.

While PG 0048+091 and PG 1315−123 are the first *K2*-observed p-mode-dominated hybrids, *K2* has observed two other p-mode sdBV stars (Reed et al. 2018a) and both of those also have main-sequence F or G companions. Only the two *K1*-observed p-mode sdBV stars appear to not be in binaries. Is this an observational selection effect (sdB stars are easier to detect when hotter and therefore brighter) or an envelope-stripping effect (main-sequence F or G companions strip off more of the sdB envelope, thereby making them hotter)?

KIC 10139564, PG 0048+091, and PG 1315−123 are hybrid pulsators while the p-mode pulsators EPIC 211823779 and LB 378, observed during C5 (Reed et al. 2018a), are not. However, EPIC 211823779 and LB 378 are both substantially fainter. Does this mean that most (or all) p-mode sdBV stars are hybrids, or is there a mix? It is possible that the Transiting Exoplanet Survey Satellite (TESS) will answer this question as it observes known p-mode pulsators that *Kepler* has not observed.

While the broad regions of power observed in some pulsations of PG 0048+091 and PG 1315−123, which we have interpreted as stochastic oscillations, are obvious in these stars, we also see

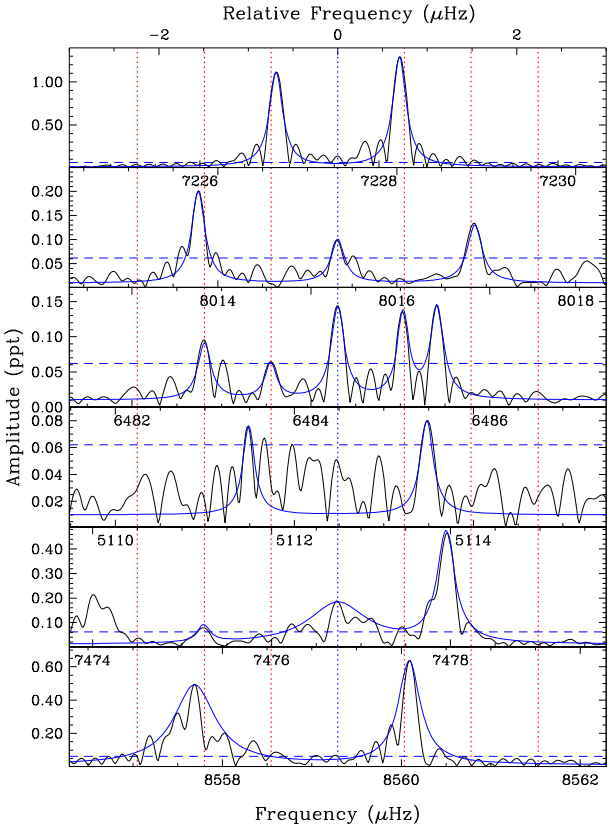

Figure 15. p-mode multiplets in PG 1315−123 stacked to compare frequency splittings. The central (blue) vertical dashed line indicates the position of the $m = 0$ component, with the other (green) vertical lines indicating successive azimuthal values at a spacing of 0.731 μHz. The clearest multiplets are shown at the top.

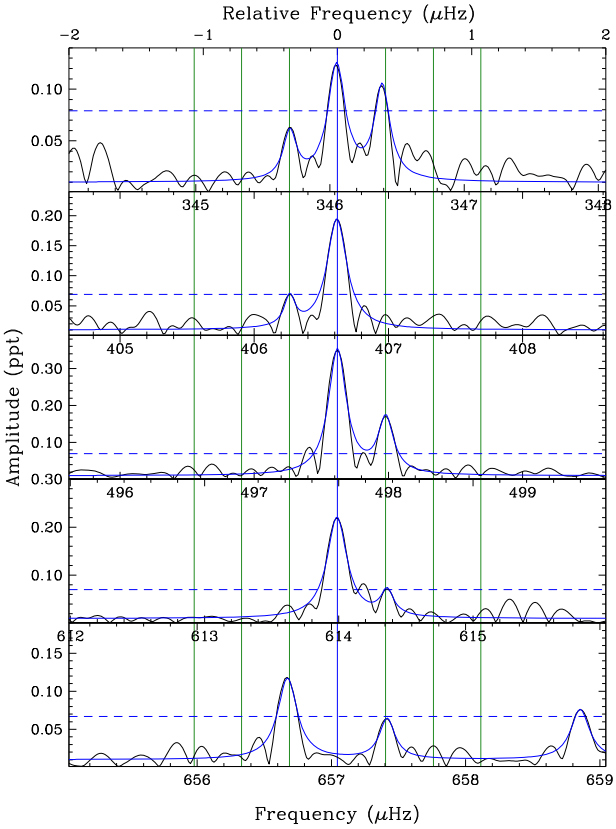

Figure 16. Possible g-mode multiplets in PG 1315−123 similar to Fig. 12. Vertical lines indicate determined $\ell = 1$ splittings of 0.358 μHz and horizontal dashed lines the detection limit. Lorentzian fits to the peaks are shown as solid (blue) lines.

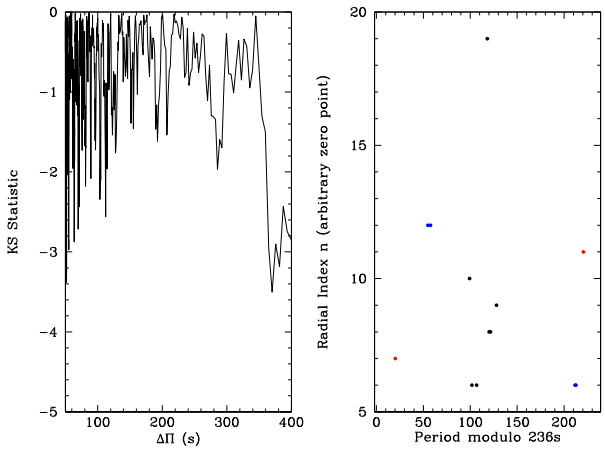

Figure 17. Same as Fig. 13 for PG 1315−123. The black points are asymptotic $\ell = 1$ modes, the blue points are $\ell = 1$ multiplets that do not fit the asymptotic sequence, and the red points are unidentified.

evidence of similar structures in other p-mode sdBV stars, including KIC 10139564 (Baran et al. 2012), KIC 3527751 (Foster et al. 2015), and Balloon 090100001 (Baran et al. 2009). Another examination of those data could be illuminating.

We also continue to find an abundance of contradictions; we now have two radially differential rotators (PG 0048+091 and KIC 3527751) with similar ratios of rotation (and a third likely differential rotator, which only has p-mode multiplets; Baran et al. 2017) and two that rotate as if they are solid bodies, two stars (KIC 10139564 and PG 0048+091) with small p-mode overtone spacings, and three that are likely similar to model predictions (PG 0048+091, KIC 3527751, and Balloon 090100001). The sdB stars in long-period binaries tend to have short rotation periods (PG 0048+091, PG 1315−123, SDSS J082003.35+173914.2, and LB 378) while those in short-period binaries tend to have longer rotation periods. The underlying physics of these phenomena has yet to be explored, but recent advances in modelling (Constantino et al. 2015; Ghasemi et al. 2017) may promote their study (e.g. Preece, Tout & Jeffery 2018).

Additional *K2*-observed pulsators (now observing C18) should help to clarify some of these issues. *K2* has now oberved about twice as many sdBV stars as *K1*. While the duration of *K2*'s campaigns is much shorter than that of *K1*'s, it is clearly sufficient for seismic interpretations of sdBV pulsations. We look forward to continued discoveries from remaining *K2* observations. Additionally, TESS should provide seismic measurements of many more sdBV stars and *Gaia* will provide accurate distances. The accumulation of space-based precision measurements, combined with spectroscopic ones, should provide tight constraints on structural and seismic models. The modern open-source MESA code, with crowd-sourced modifications and updates, is allowing for interesting investigations, which should continue to improve our knowledge of sdB stars and post-He flash stars in general.

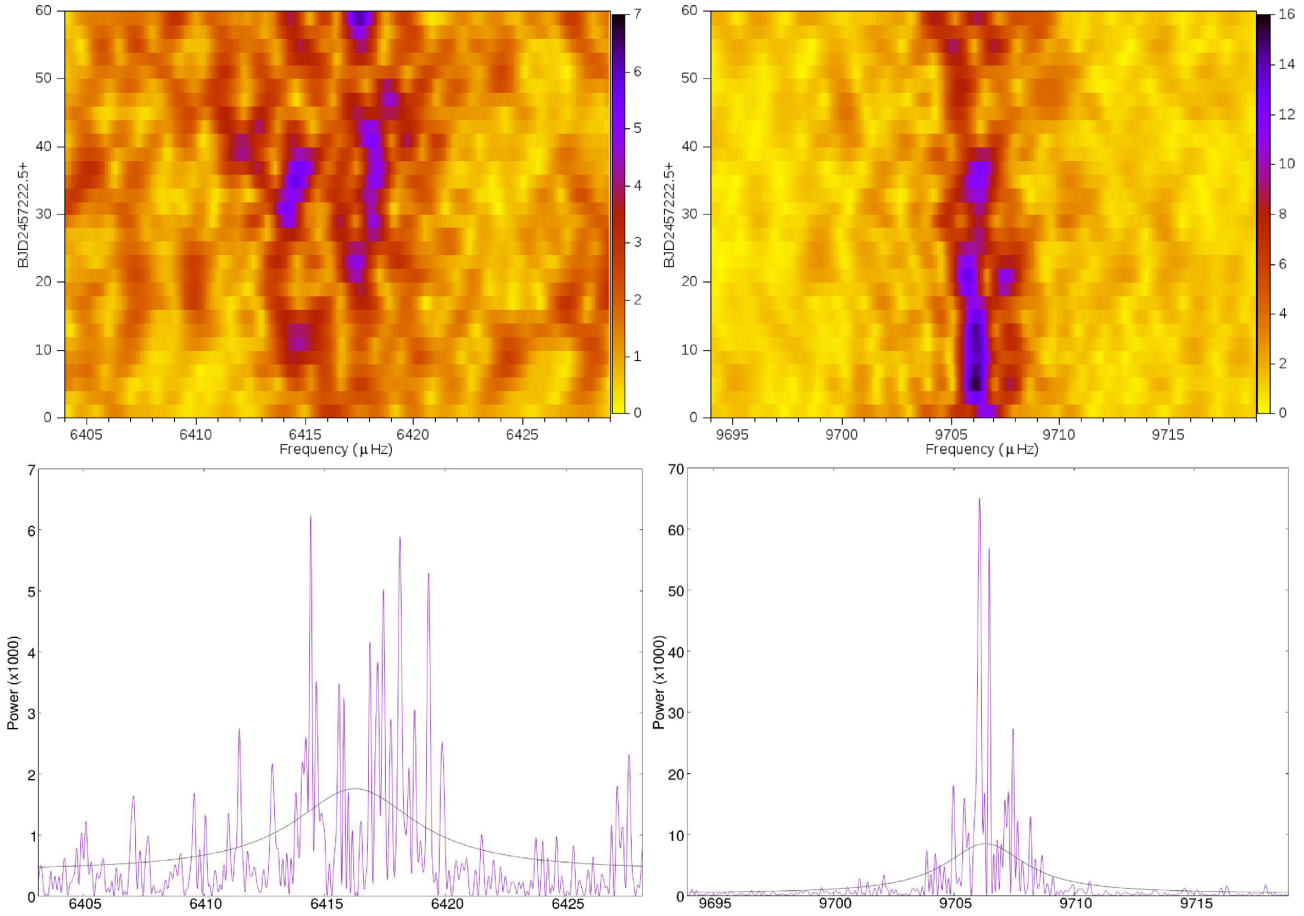

Figure 18. Fourier transforms like Fig. 14 for PG 1315−123 showing two regions with stochastic pulsation properties.

Table 9. Lorentzian widths fitted to observations of PG 1315−123.

Freq (μHz)	LW (μHz)	H_i (ppt^2)	Freq (μHz)	LW (μHz)	H_i (ppt^2)
6417	3.1	1.4	8811	5.5	4.9
8114	3.1	26.0	9706	2.1	8.2

ACKNOWLEDGEMENTS

Funding for this research was provided by the National Science Foundation grant #1312869 and NASA grant 14-K2GO2-2-0047 as part of the *K2* guest observer programme. Any opinions, findings, and conclusions or recommendations expressed in this material are those of the authors and do not necessarily reflect the views of the National Science Foundation or NASA. JAC was funded by the Missouri Space Grant, which is funded by NASA. ASB gratefully acknowledges financial support from the Polish National Science Center under project No. UMO-2017/26/E/ST9/00703. This paper includes data obtained by the *Kepler* mission. Funding for the *Kepler* mission is provided by the NASA Science Mission directorate. Data presented in this paper were obtained from the Mikulski Archive for Space Telescopes (MAST). STScI is operated by the Association of Universities for Research in Astronomy, Inc., under NASA contract NAS5-26555. Support for MAST for non-HST data is provided by the NASA Office of Space Science via grant NNX13AC07G and by other grants and contracts.

Some of the spectroscopic observations used in this work were obtained with the Nordic Optical Telescope at the Observatorio del Roque de los Muchachos and operated jointly by Denmark, Finland, Iceland, Norway, and Sweden.

Based on observations collected at the European Organization for Astronomical Research in the Southern Hemisphere under ESO programmes 088.D-0364(A), 093.D-0629 (A), 096.D-0180(A), 097.D-0110(A), 098.D-0018(A), 099.D-0014(A) and 0100.D-0082(A). JV acknowledges financial support from FONDECYT grant number 3160504. This work has made use of data from the European Space Agency (ESA) mission *Gaia* (https://www.cosmos.esa.int/gaia), processed by the *Gaia* Data Processing and Analysis Consortium (DPAC, https://www.cosmos.esa.int/web/gaia/dpac/consortium). Funding for DPAC has been provided by national institutions, in particular the institutions participating in the *Gaia* Multilateral Agreement. This publication makes use of data products from the Two Micron All Sky Survey, which is a joint project of the University of Massachusetts and the Infrared Processing and Analysis Centre/California Institute of Technology, funded by the National Aeronautics and Space Administration and the National Science Foundation. This research was made possible through the use of the AAVSO Photometric All-Sky Survey (APASS), funded by the Robert Martin Ayers Sciences Fund. P.N. acknowledges support from the Grant Agency of the Czech Republic (18-20083S). This research has used the services of ASTROSERVER.ORG under reference B7XWR0.

REFERENCES

Bailer-Jones C. A. L., Rybizki J., Fouesneau M., Mantelet G., Andrae R., 2018, AJ, 156, 58
Baran A. et al., 2009, MNRAS, 392, 1092
Baran A. S. et al., 2012, MNRAS, 424, 2686
Baran A. S., Reed M. D., Østensen R. H., Telting J. H., Jeffery C. S., 2017, A&A, 597, A95
Bevington P. R., Robinson D. K., 2003, Data Reduction and Error Analysis for the Physical Sciences. McGraw-Hill, New York, NY
Bohlin R. C., Mészáros S., Fleming S. W., Gordon K. D., Koekemoer A. M., Kovács J., 2017, AJ, 153, 234
Bowman D. M., Kurtz D. W., 2018, MNRAS, 476, 3169
Charpinet S., Fontaine G., Brassard P., Dorman B., 2000, ApJS, 131, 223
Charpinet S., Brassard P., Van Grootel V., Fontaine G., 2014, in van Grootel V., Green E., Fontaine G., Charpinet S., eds, ASP Conf. Ser., Vol. 481, 6th Meeting on Hot Subdwarf Stars and Related Objects. Astron. Soc. Pac., San Francisco, p. 179
Constantino T., Campbell S., Christensen-Dalsgaard J., Lattanzio J., Stello D., 2015, MNRAS, 452, 123
Cutri R. M. et al., 2012, Explanatory Supplement to the WISE All-Sky Data Release Products
Degroote P. et al., 2010, Nature, 464, 259
Djupvik A. A., Andersen J., 2010, in Diego J. M., Goicoechea L., González-Serrano J. I., Gorgas J., eds, Astrophysics and Space Science Proceedings, Vol. 14, Highlights of Spanish Astrophysics V. Springer-Verlag, Berlin, p. 211
Evans D. W. et al., 2018, A&A, 616A, 4E
Foreman-Mackey D., Hogg D. W., Lang D., Goodman J., 2013, PASP, 125, 306
Foster H. M., Reed M. D., Telting J. H., Østensen R. H., Baran A. S., 2015, ApJ, 805, 94
Gaia Collaboration, 2016, A&A, 595, A1
Gaia Collaboration, 2018, A&A, 616A, 1G
Ghasemi H., Moravveji E., Aerts C., Safari H., Vuckovic M., 2017, MNRAS, 465, 1518
Green R. F., Schmidt M., Liebert J., 1986, ApJS, 61, 305
Guggenberger E., Hekker S., Basu S., Bellinger E., 2016, MNRAS, 460, 4277
Heber U., 2016, PASP, 128, 082001
Hbeny I., Lanz T., 2017, preprint (arXiv:1706.01859)
Huber D. et al., 2016, ApJS, 224, 2
Ketzer L., Reed M. D., Baran A. S., Németh P., Telting J. H., Østensen R. H., Jeffery C. S., 2017, MNRAS, 467, 461
Koen C., O'Donoghue D., Kilkenny D., Pollacco D. L., 2004, New Astron., 9, 565
Kurucz R. L., 1979, ApJS, 40, 1
Larsen J., Modigliani A., Bramich D., 2012, Very Large Telescope UVES Pipeline User's Manual, VLT-MAN-ESO-19500-2965. p. 1
Lindegren L. et al., 2018, A&A, 616A, 2L
Metcalfe T. S., Montgomery M. H., Kanaan A., 2004, ApJ, 605, L133
Németh P., Kawka A., Vennes S., 2012, MNRAS, 427, 2180
Pesnell W. D., 1985, ApJ, 292, 238
Preece H. P., Tout C. A., Jeffery C. S., 2018, MNRAS, 481, 715
Reed M. D. et al., 2007, ApJ, 664, 518
Reed M. D. et al., 2010, MNRAS, 409, 1496
Reed M. D. et al., 2018a, MNRAS, 474, 5186
Reed M. D. et al., 2018b, Open Astron., 27, 157
Reed M. D. et al., 2011, MNRAS, 414, 2885
Riello M. et al., 2018, A&A, 616A, 3R
Shulyak D., Tsymbal V., Ryabchikova T., Stütz C., Weiss W. W., 2004, A&A, 428, 993
Skrutskie M. F. et al., 2006, AJ, 131, 1163
Telting J. H., Østensen R. H., Oreiro R., Reed M., Farris L., O'Toole S., Aerts C., 2012, in Kilkenny D., Jeffery C. S., Koen C., eds, ASP Conf. Ser., Vol. 452, Fifth Meeting on Hot Subdwarf Stars and Related Objects. Astron. Soc. Pac., San Francisco, p. 147
Tkachenko A., 2015, A&A, 581, A129
Tsymbal V., 1996, in Adelman S. J., Kupka F., Weiss W. W., eds, ASP Conf. Ser., Vol. 108, M.A.S.S., Model Atmospheres and Spectrum Synthesis. Astron. Soc. Pac., San Francisco, p. 198
Vos J., Østensen R. H., Németh P., Green E. M., Heber U., Van Winckel H., 2013, A&A, 559, A54Paper II
Vos J., Németh P., Vučković M., Østensen R., Parsons S., 2018, MNRAS, 473, 693
Werner K., Deetjen J. L., Dreizler S., Nagel T., Rauch T., Schuh S. L., 2003, in Hubeny I., Mihalas D., Werner K., eds, ASP Conf. Ser., Vol. 288, Stellar Atmosphere Modeling. Astron. Soc. Pac., San Francisco, p. 31
Østensen R. H., Reed M. D., Baran A. S., Telting J. H., 2014a, A&A, 564, L14
Østensen R. H., Telting J. H., Reed M. D., Baran A. S., Nemeth P., Kiaeerad F., 2014b, A&A, 569, A15

This paper has been typeset from a TEX/LATEX file prepared by the author.